Research Updates

Radiative cooling for energy sustainability: Materials, systems, and applications

Lyu Zhou,[1,2] Jacob Rada,[1,2] Yanpei Tian,[1] Yu Han,[3] Zhiping Lai,[3] Matthew F. McCabe,[4] and Qiaoqiang Gan[1,2,*]

[1]*Material Science Engineering, Physical Science Engineering Division, King Abdullah University of Science and Technology (KAUST), Thuwal, Saudi Arabia*

[2]*Electrical Engineering, University at Buffalo, The State University of New York, Buffalo, New York 14260, USA*

[3]*Advanced Membranes and Porous Materials Center, Physical Sciences and Engineering Division, King Abdullah University of Science and Technology (KAUST), Thuwal, Saudi Arabia*

[4]*Division of Biological and Environmental Science and Engineering (BESE), King Abdullah University of Science and Technology (KAUST), Thuwal, Saudi Arabia*

(Received 26 April 2022; revised 21 July 2022; accepted 25 July 2022; published 20 September 2022)

As a sustainable technology, radiative cooling has received considerable attention due to its potential in energy sustainability. Unlike conventional cooling techniques, radiative cooling does not consume electricity during its operation and is therefore particularly attractive in reducing the energy demand for cooling and addressing global warming by reducing carbon emissions. The general principle requires a radiative cooler to be thermally emissive to dissipate heat via thermal radiation. During the daytime, the cooler needs to minimize the solar heating effect to ensure subambient temperatures. Guided by these criteria, researchers have developed various materials with engineered optical, thermal, and mechanical features. In this review, we will first explore the fundamentals of heat transfer in radiative cooling processes. Subsequently, we will summarize the state-of-the-art progress on material synthesis and system designs. Building upon those recently developed features, we will review how this technology has been implemented in practical applications, ranging from thermal management of buildings, semiconductor cooling, personal comfort design, and atmospheric water harvesting. Finally, we will conclude this review by identifying and discussing some of the remaining challenges requiring future research and development.

DOI: 10.1103/PhysRevMaterials.6.090201

I. INTRODUCTION

Since ancient times, when people first started to utilize ice for food storage [1], the development of cooling technologies has often moved in parallel with the advancement of society. In modern life, cooling strongly impacts our daily routines in numerous ways via air conditioning, personal thermal regulation, energy generation, and thermal management for electronic devices [2]. However, the energy consumption for cooling has significantly increased as well. According to the Annual Energy Outlook released by U.S. Energy Information Administration (EIA), electricity used for cooling the interior space of buildings was nearly 389 billion kWh, which amounts to 10% of the total electricity consumed in the U.S. in 2021 [3]. Of considerable concern, most current cooling technologies, such as air-compressor-based cooling systems, directly or indirectly emit a massive amount of carbon dioxide, exacerbating the consequences of climate change [4]. To meet the rapidly growing need for cooling while reducing the threats resulting from global warming, there is an urgent need for researchers to move toward more sustainable and efficient cooling technologies.

In recent years, there has been an emerging interest in passive radiative cooling (PRC) as a potential solution to this challenge [4]. The process relies mostly on spontaneous thermal emission from the heat source. As a result, an operating radiative cooling system does not consume any electricity nor produce carbon dioxide emissions. Compared with conventional cooling technologies such as air conditioning and evaporative cooling, a PRC system can achieve high-energy efficiency while realizing a minimal carbon footprint [4], which makes it very promising for carbon reduction goals established by the Paris Agreement [5]. Importantly, a radiative cooling design normally only comprises a thin film coating with thicknesses often <1 cm. Therefore, this simple structure can be easily integrated with existing infrastructures without adding system complexity [6].

In the past decades, many pioneering works have reported on subambient nighttime cooling using black emitters [7–12]. However, realizing subambient daytime cooling remained a challenge, as intense solar radiation can rapidly heat up a black emitter. As such, carefully controlling the absorptivity spectra of the emitter is essential to realizing passive daytime radiative cooling [13]. In general, it is necessary to minimize solar absorption, while maximizing thermal emission. Following these criteria, numerous studies were

*qiaoqiang.gan@kaust.edu.sa

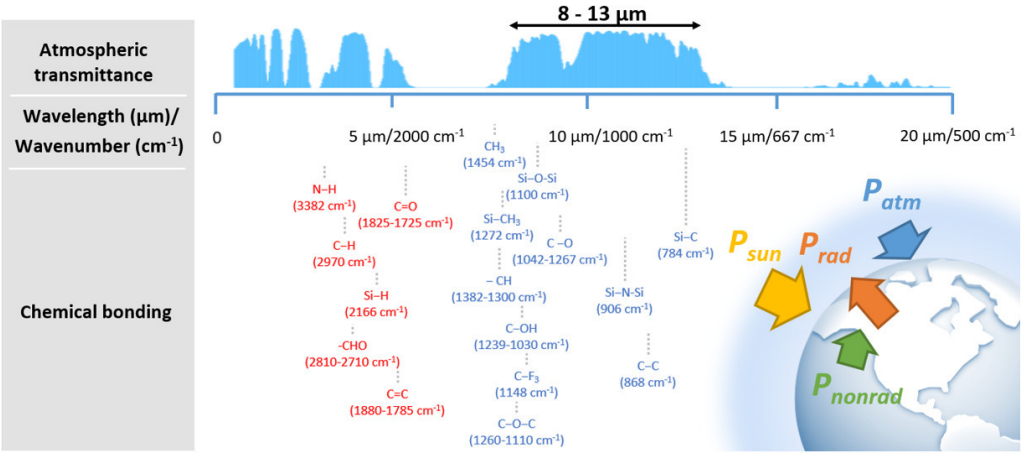

FIG. 1. (upper) Atmospheric transmittance as a function of wavelength and wave number. The arrow highlights the prior atmospheric transparency window between 8 and 13 μm. (lower) Functional groups reported in previous works and their corresponding positions in the wave number range. The chemical bonds located before 8 μm are highlighted in red, and the bonds located between 8 and 13 μm are highlighted in blue.

performed to develop selective emitters for daytime radiative cooling [4,6,14–29]. In this review, we will overview the latest progress in this active area by summarizing research considerations regarding material synthesis, system design, and application developments. Specifically, we will first discuss the fundamentals and principles of daytime radiative cooling (Sec. II). Then in Sec. III, we will summarize the recent works for cooling materials investigation. In Sec. IV, we will examine the system design of radiative cooling, which has been overlooked in previous review articles. Finally, we will discuss different applications of radiative cooling in Sec. V and provide a general outlook for future research in Sec. VI.

II. HEAT FLUX OF RADIATIVE COOLING: FUNDAMENTAL PRINCIPLES

In principle, thermal radiation is spontaneously emitted from any thermal object at a temperature >0 K via electromagnetic waves [30]. According to Kirchhoff's law of thermal radiation, all bodies are both thermal emitters and receivers with identical efficiencies, i.e., the emissivity always equals the absorptivity at thermal equilibrium. Radiative cooling is a technology that builds upon these well-established concepts [4]. Through the atmospheric transparency window (e.g., 8–13 μm in wavelength, Fig. 1), an object on the surface of Earth dissipates heat via thermal radiation (P_{rad}) because its temperature (~300 K) is normally much higher than outer space (3 K). On the other hand, the object absorbs thermal radiation from both the atmosphere (P_{atm}) and solar irradiance (P_{sun}) during the daytime. Furthermore, it also exchanges heat with the environment through nonradiative processes, such as convection and conduction. As a result, the heat flux of radiative cooling (P_{net}) can be described as follows:

$$P_{\text{net}} = P_{\text{rad}} - P_{\text{atm}} - P_{\text{sun}} - P_{\text{nonrad}}. \quad (1)$$

These combined factors determine the equilibrium temperature of the emitter when $P_{\text{net}} = 0$. In general, to obtain subambient cooling effect during the daytime, it is always desired to minimize the absorbed heat from the environment (P_{atm} and P_{sun}) while simultaneously maximizing the emitted heat from the emitter (P_{rad}). In the following subsection, we will discuss these heat flux components in more detail.

A. Thermal radiation from the emitter (P_{rad})

At thermodynamic equilibrium, the spectral radiation of a blackbody can be described by Planck's law [Eq. (2)]:

$$I_{BB}(T,\ \lambda) = \frac{2hc^2}{\lambda^5}\frac{1}{\exp\left(\frac{hc}{\lambda k_B T}\right) - 1}, \quad (2)$$

where T is the temperature of the blackbody, h is Planck's constant, k_B is the Boltzmann constant, c is the speed of light, and λ is the wavelength. Based on Eq. (2), the thermal emission from an emitter is mainly determined by its thermal equilibrium temperature (T_{rad}) and emissivity profile (ε_{rad}), as given by

$$P_{\text{rad}}(T_{\text{rad}}) = A\int d\Omega\cos(\theta)\int d\lambda I_{BB}(T_{\text{rad}},\ \lambda)\varepsilon_{\text{rad}}(\theta,\ \lambda), \quad (3)$$

where A is the area size of the emitting surface, $\int d$ is the angular integral of the emitter over accessible space, and ε_{rad} is the spectral emissivity of the emitter. In general, unity emissivity is desired to maximize the outgoing thermal radiation. However, in an outdoor environment, an emitter also absorbs external thermal radiation, especially from the atmosphere. Depending on the temperature of the environment, researchers have developed broadband and narrowband emitters to obtain optimized cooling performance, both of which will be discussed in detail in the following two subsections.

1. Broadband vs narrowband emitters

When designing an emitter for radiative cooling, the most important criteria to consider is the spectral selectivity of the emitter. Within the visible (VIS) and near-infrared (NIR) range (i.e., 380–2500 nm), the solar absorptivity of an emitter is required to be <10% to realize a subambient cooling effect [13]. Furthermore, depending on the direction of net heat flux,

either a broadband or narrowband emitter is preferred for optimized cooling performance [6]. For example, when the equilibrium temperature of the emitter is below ambient, the net heat flux flows from the environment to the emitter. In such cases, an emitter that has unity absorption only within 8 to 13 μm shows better cooling performance, as the narrowband emissivity profile suppresses the heat absorption from the atmosphere. This situation is mostly seen in applications of refrigeration and food storage [31]. On the other hand, when the emitter's equilibrium temperature is above ambient, i.e., the net heat flux flows from the emitter to the environment, a broadband emitter that has unity emissivity beyond 4 μm is preferred due to the higher heat transfer efficiency. This situation can be found in cooling applications for solar modules [27], building envelopes [21–23], and the thermal management of the human body [24–26]. By carefully selecting the materials and designs, researchers can obtain optimized cooling performance in the corresponding conditions, as will be discussed below.

2. Material selection and structural design

Typical metal oxides, such as titanium dioxide (TiO_2), silicon dioxide (SiO_2), and zinc oxide (ZnO), have been frequently deployed with polymeric binders for cooling paints throughout the last century [32–34]. Due to the strong inherent thermal emission of the binders and solar scattering effect introduced by the embedded particles, researchers developed efficient painting materials for radiative cooling during the night and reduced surface temperature throughout the day [35]. However, intrinsic limitations exist for these materials to realize subambient daytime radiative cooling. For example, TiO_2 has high absorptivity within 300–410 nm, which will introduce a strong solar heating effect [36]. SiO_2 exhibits a sudden change of refractive index ~9 μm, resulting in a strong reflection peak within the atmospheric window [37]. These issues can be partially addressed by optimizing the structure design, such as by tuning the particle sizes [38], adding polymer binders [30,36], or introducing wide optical bandgap dielectric particles like aluminum oxide (Al_2O_3), calcium carbonate ($CaCO_3$), and barium sulfate ($BaSO_4$) [36,39–42]. Additionally, one can reduce the solar absorption and enhance the thermal emission by introducing interferometer structures, as will be discussed in Secs. III A and III E.

On the other hand, polymers are recognized as promising alternatives for radiative cooling due to their scalability and low cost. These materials normally contain many functional groups or bonds that correspond to absorption in the long-wavelength infrared (LWIR) range. By carefully selecting polymer materials that contain functional groups at desired wavelengths, one can demonstrate an efficient cooling effect using simple two-layered structures [43–45]. For example, double-bond functional groups like C = C and C = O have higher absorptivity in the range of 2000–1500 cm^{-1} (corresponding to 4–6.7μm) owing to stretching vibration. Therefore, for materials like polymethyl methacrylate (PMMA) that contain C = O functional groups, their absorption peaks ~6 μm can support strong thermal emission [46]. Figure 1 shows typical chemical bonds within 2–20 μm (5000–500 cm^{-1}) corresponding to the atmospheric transmission window [43–48]. These functional groups within and beyond the 8–13 μm range are highlighted in blue and red, respectively. Based on this chart, researchers can select polymers that are applicable to situations where either a broadband or narrowband emitter will provide the best cooling performance. A more comprehensive exploration of these materials has been published elsewhere [43].

B. Absorbed atmospheric radiation (P_{atm})

Radiative cooling has also been referred to as sky cooling since heat is transported through the clear sky to outer space via radiation. In general, the atmospheric radiation absorbed by a thermal emitter can be estimated by

$$P_{atm}(T_{amb}) = A \int d\Omega \cos(\theta) \int d\lambda I_{BB}(T_{amb}, \lambda)\varepsilon_{rad} \times (\theta, \lambda)\varepsilon_{atm}(\theta, \lambda), \quad (4)$$

where T_{amb} is the temperature of ambient air, and ε_{atm} is the spectral emissivity of the atmosphere. Given transmittance in the zenith direction $\tau_{atm}(0, \lambda)$, the angular atmospheric emissivity ε_{atm} at the zenith angle (θ) can be estimated by

$$\varepsilon_{atm}(\theta, \lambda) = 1 - [\tau_{atm}(0, \lambda)]^{1/\cos\theta}. \quad (5)$$

However, due to the intrinsic absorption of atmospheric gas components, such as carbon dioxide (CO_2), ozone (O_3), and water vapor (H_2O) [49], the atmosphere exhibits only a few discrete transparency bands within 0.3–20 μm (Fig. 1). The transparency band located between 8 and 13 μm is the most significant, as it coincidently aligns with the peak of blackbody radiation at 300 K (~9 μm). Other transparency bands also exist that contribute to radiative cooling in dry weather, one of which is in the LWIR region of 17.2–25 μm [50,51]. The transmissivity of these bands is largely dependent on the weather conditions, such as temperature, relative humidity, cloud cover, and latitude [6,52,53]. Among all weather factors, two of the most important ones are the atmospheric temperature and relative humidity, as they have the largest impact on atmospheric LWIR transmissivity. Many works developed simplified models to estimate the equivalent atmospheric transmissivity, as summarized in a previous review [21]. For example, the widely used MODTRAN model provides the capacity to adjust a variety of different environmental factors and has been used to model the atmospheric transmittance [53–63]. As shown in Fig. 2(a), the atmospheric transmittance was modeled with different ambient temperatures and relative humidity [63]. These results show that, when the environment changes from 0 °C/RH 50% to 40 °C/100%, the atmospheric transmittance decreases by nearly half within the 8–13 μm range and to zero within the 17.2–25 μm range. This reduction in atmospheric transmittance will result in a significant decrease in cooling performance.

As shown in Fig. 2(b), when the ambient temperature is 294.2 K and the surface relative humidity (RH) is 20%, the cooling power potential of a blackbody emitter is 102.7 W/m^2 within 750–1400 cm^{-1} (7.14–13.33 μm) and 4.5 W/m^2 within 400–580 cm^{-1} (17.2–25 μm) [51]. In areas that consistently have extremely low humidity, the cooling power of an emitter will be more accurately determined by considering the atmospheric transparency windows at both 8–13 μm and 17.2–25 μm [49]. To illustrate this effect in the real

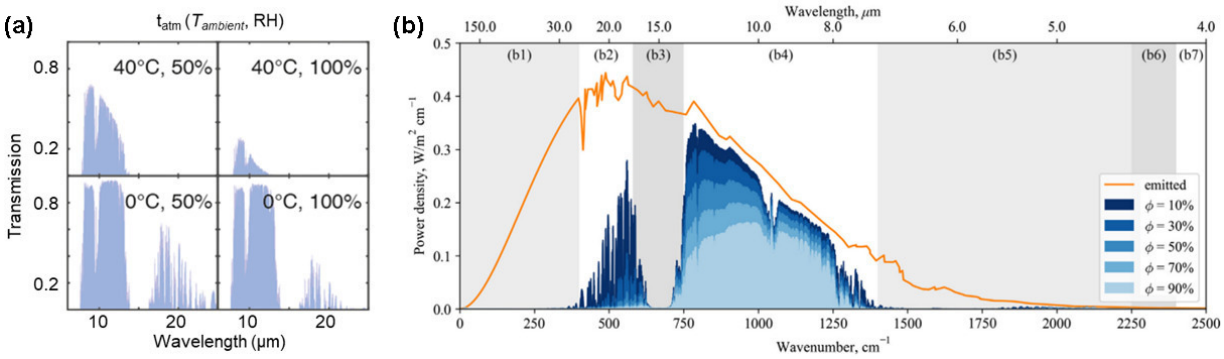

FIG. 2. (a) Modeled atmospheric transmission in different temperature and relative humidity conditions. Copyright 2020 American Chemical Society (Ref. [63]). (b) The cooling power potential from a blackbody emitter by considering the atmospheric transparency bands within different wavelength ranges (blue shades). The different shades of blue represent the effect of relative humidity on atmospheric thermal radiance/emission. Copyright 2019 Elsevier (Ref. [51]).

world, a cooling power of 40.1 W/m^2 was demonstrated using a spectrally selective emitter in California [31], while a minor cooling effect was observed in Hong Kong using an identical design due to the humid local environment [56]. By studying the effect of relative humidity on radiative cooling power, one can see that there is a need to tailor the system design with respect to the typical absorbed atmospheric radiation, as will be discussed in Sec. IV.

C. Absorbed solar irradiation (P_{sun})

The most significant factor that hinders radiative cooling is solar radiation. The complete solar spectrum covers the ultraviolet (UV; 250–380 nm), VIS (380–750 nm), and NIR (750–2500 nm) ranges. Under air mass (AM) 1.5 solar irradiation, the total irradiance ($I_{AM1.5}$) of sunlight is ~1000 W/m^2. The UV, VIS, and NIR bands constitute 6.8, 44.7, and 48.5% of the AM1.5 spectral power density, respectively. On the other hand, the typical cooling power of a radiative emitter at ambient temperature is ~100 W/m^2. Therefore, to realize subambient daytime radiative cooling, it requires the emitter to have a minimized absorption in all three ranges but especially in the VIS and NIR ranges. In general, the absorbed solar irradiation power (P_{sun}) of an emitter is given by

$$P_{sun} = A\cos(\alpha)\int d\lambda I_{AM1.5}(\lambda)\varepsilon_{rad\_solar}(\theta,\ \lambda). \quad (6)$$

Here the angle α refers to the angle between the incident solar direction and the normal direction of the emitting surface. The absorptivity of the emitting surface within the solar spectral range equals to the emissivity, which is given by $\varepsilon_{rad\_solar}(\theta,\ \lambda)$. In recent studies, researchers developed emitters with minimized solar absorptivity, with some studies realizing a total absorption of <5% [64,65]. In addition, suppressed solar absorption can also be obtained by implementing sunshades [44,55,66] or solar filters [67,68]. Although these methods can introduce additional complexity to the system, they can also serve a secondary purpose including thermal insulation [68] and beam steering [44], as will be discussed in Sec. IV.

D. Conduction and convection (P_{nonrad})

Nonradiative heat losses via thermal conduction and convection also play an important role in the heat flux of radiative cooling [i.e., P_{net} in Eq. (1)]. The heat flux of nonradiative heat exchange P_{nonrad} can be expressed by

$$P_{nonrad} = Aq(T_{amb} - T_{rad}),$$

where q represents the nonradiative heat transfer coefficient. Depending on the temperature difference between the emitting surface (T_{rad}) and ambient air (T_{amb}), the nonradiative heat loss can either be beneficial or detrimental. For example, most photovoltaic (PV) plants operate at a temperature that is much higher than ambient. In this case, a strong conduction or convection heat transfer will facilitate heat dissipation [69,70]. On the other hand, for radiative cooling research focused on subambient cooling, it is highly desired to minimize P_{nonrad} to obtain lower temperatures. In most studies, researchers employed polyethylene (PE) films and thermally insulating containers (e.g., polyester foam boxes) to minimize the nonradiative heat transfer. Advanced techniques, such as aerogels [68] and vacuum chambers [31] were also employed to explore the upper limit of radiative cooling, as will be discussed in Sec. IV.

III. MATERIAL DESIGN PRINCIPLES

In this section, we will review recent works that realized daytime radiative cooling based on different mechanisms and/or structures.

A. Spectral selectivity for radiative cooling

According to Secs. II A and II C, one of the major challenges with material design for passive daytime cooling is developing a surface that possesses a near unity solar reflectance (for minimizing solar heating gain) and a high thermal emittance (for maximizing radiative heat loss) [4,13–21]. For practical applications, to achieve better cooling performance or even a subambient cooling effect, the solar reflectance needs to be >90%, preferably even >95%, to minimize the solar heating effect. Numerous materials have been reported to realize this spectrally selective feature over

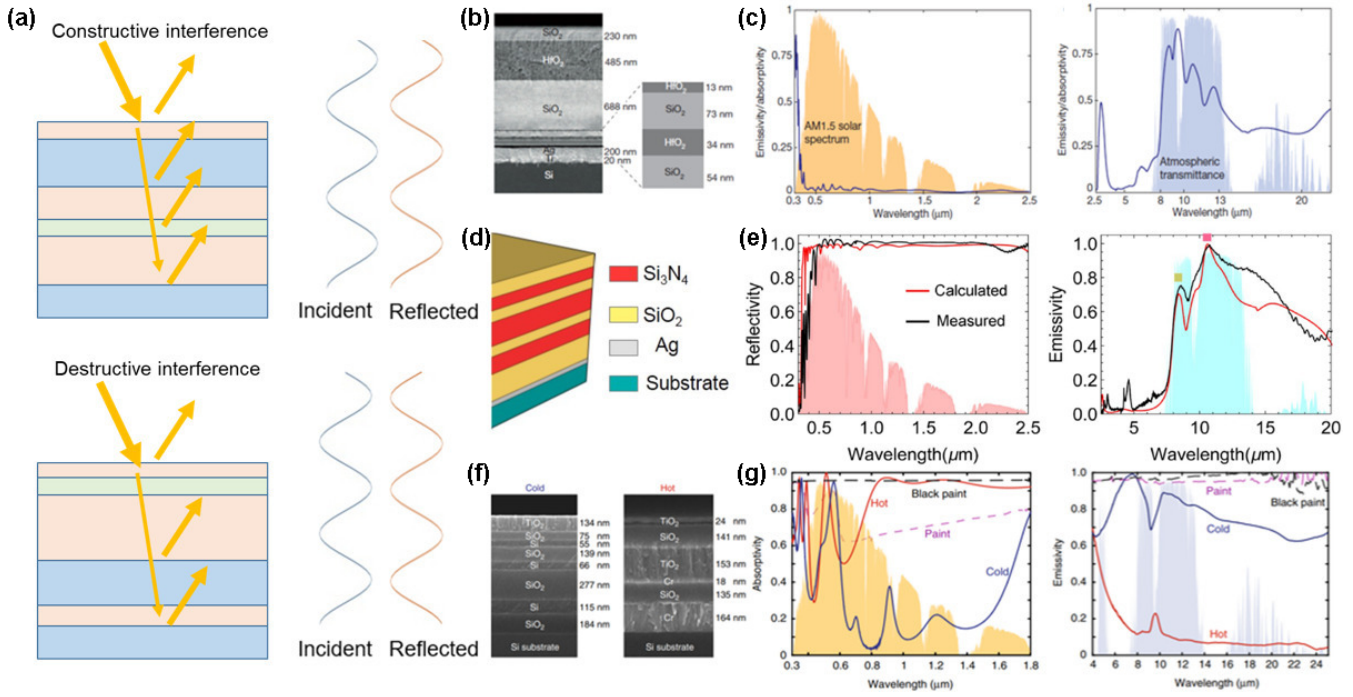

FIG. 3. (a) Schematic illustrations of constructive interference and destructive interference. (b) and (c) The seven-layered SiO_2/HfO_2 interference structure and its measured spectra in the visible (VIS)-near infrared (NIR) and midinfrared (MIR) ranges. Copyright 2014, Springer Nature (Ref. [13]). (d) and (e) The alternating Si_3N_4/SiO_2 interference structure and its measured spectra in the VIS-NIR and MIR ranges. Copyright 2020, Elsevier (Ref. [87]). (f) and (g). Interference photonic structures for both cold and hot thermal management and their measured spectra in the VIS-NIR and MIR ranges. Copyright 2018, Springer Nature (Ref. [107]).

two different wavelength regions in the VIS-to-NIR, and midinfrared (MIR) regimes [13,31,36,38–175]. For instance, spectrally selective radiative cooling was found in natural creatures (e.g., butterflies [103] and silver ants [104]). Inspired by these naturally existing cooling materials, multilayered photonic structures were reported with top thermal radiation layers and bottom solar reflective metals [13,42,44,87–102]. The metal layer [usually silver (Ag)] can reflect the sunlight to reduce the solar heat gain while the top thin film interference is designed to enhance the thermal emittance over the atmospheric window. Bilayer metasurfaces with patterned structures were also reported for tailoring the spectral emittance of the surface over the atmospheric window. These structures are transparent over solar wavelengths to allow sunlight to be reflected by the bottom metal layer [105]. Additionally, porous structures with light-scattering air voids generated by hierarchically ordered pores or fibers can increase the optical performance for a better cooling effect [64,65]. The strong backscattering of sunlight happens at the interface between air voids. Those porous walls or fibers increase the solar reflectance. A randomly distributed structure is another approach to achieving such spectral selectivity. Generally, the bottom reflective metal layer provides high solar reflectance, while the randomly distributed layer with inorganic particles, such as SiO_2, TiO_2, $CaCO_3$, $BaSO_4$, or Al_2O_3, is responsible for high thermal emittance due to the overlap between their infrared molecular vibrations and the atmospheric window. The polymer is usually employed as the matrix to bind these particles for scalable deployment, which can be found in many commercially available paints and pigments. In the following subsections, we will summarize major types of materials to realize this required spectral selectivity for radiative cooling.

B. Constructive or destructive interference

Thin film interferometers have been studied extensively for manipulating light absorption or reflection [80]. By arranging thin film materials with proper thickness and sequence, constructive or destructive interference conditions can be met within a wide wavelength range, resulting in different optical responses [Fig. 3(a)] [81,82]. In recent years, the research interests of multilayered thin film interference have merged with thermal applications, whereby a carefully designed structure can meet the stringent spectral selectivity requirements for radiative cooling [13,31,87–102]. An alternating layered structure was reported to realize subambient cooling under direct sunlight exposure [Fig. 3(b)] [13]. The layered structure is composed of two parts: the top thermal radiation layer consists of three thick, alternating layers of SiO_2 and hafnium dioxide (HfO_2), while the bottom solar reflection layer consists of four alternating layers of HfO_2 and SiO_2. This multilayered film exhibited a solar reflectivity of up to 97% [Fig. 3(c)]. Additionally, the phonon polariton resonance of SiO_2 and the interference introduced by the layered structure lead to a strong emissivity within the 8–13 μm range. Remarkably, the emitter achieves an average temperature reduction of 4.9 °C under a solar irradiance of 850 W/m^2. Another example of an interference structure uses alternated SiO_2 and silicon nitride (Si_3N_4) [Fig. 3(d)] [87]. By stacking these two materials in a

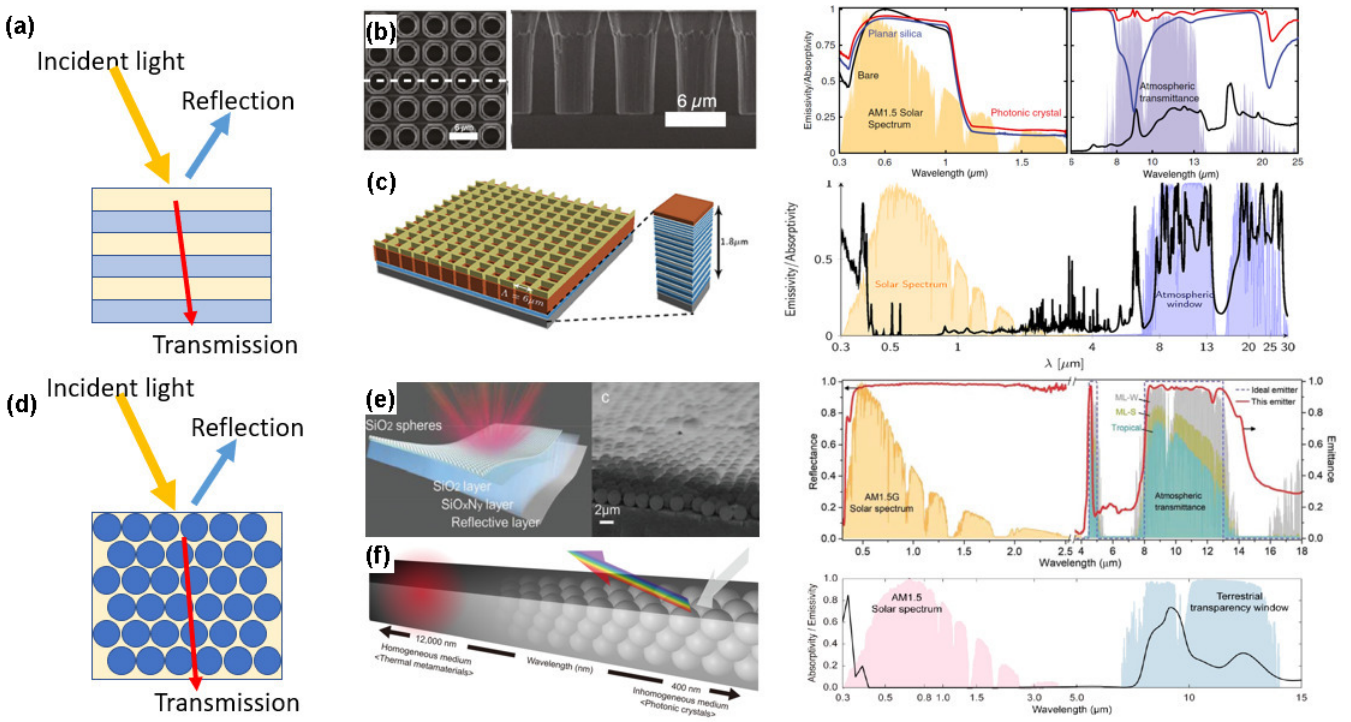

FIG. 4. (a) Schematic illustrations of a one-dimensional (1D) photonic crystal. (b) The transparent photonic coating for radiative cooling on solar absorbers and their corresponding spectra in the visible (VIS)-near infrared (NIR) and midinfrared (MIR) ranges. Copyright 2015 National Academy of Sciences (Ref. [105]). (c) A periodic quartz/Si_3N_4 square integrated with a multilayered reflector and its modeled emissivity spectra. Copyright 2013 American Chemical Society (Ref. [110]). (d) Schematic illustration of self-assembled opals. (e) Self-assembled SiO_2 spheres coated on silicon oxynitride layer and its emissivity spectrum. Copyright 2022 Wiley (Ref. [76]). (f) Schematic of a self-assembled silica opal structure and its emissivity spectra. Copyright 2020 American Chemical Society (Ref. [111]).

specific order with an optimized thickness, the layered structure exhibits ultrahigh reflection in a broad range of the solar spectrum, while emitting thermal radiation within the LWIR range only [Fig. 3(e)]. As a result, a temperature reduction of 8 °C under a solar irradiance of $\sim 900 W/m^2$ was realized. Optimization of interference effects for radiative cooling is still under investigation using numerical modeling to reveal the theoretical potential for layered structures constructed by different material selections [96,97].

Intriguingly, multilayered thin film structures have also attracted interest in structural color due to their distinctive tunability [84]. However, colored surfaces will introduce an inevitable solar heating effect for building envelopes and automobile coatings [99–101]. Although researchers have developed cool paints that can reduce the solar absorption in the NIR range [106], its cooling effect may be further improved by incorporating radiative cooling. For example, two structures with the same color (pink) but different thermal responses were reported [107]: The cold structure consists of multiple alternating layers of SiO_2 and Si, topped by a TiO_2 layer [Fig. 3(f)]. Compared with the hot structure, the cold one exhibits not only lower absorption in the NIR range but also higher thermal emittance in the MIR range for radiative cooling [Fig. 3(g)]. As a result, under a solar irradiance of $1000 W/m^2$, the cold structure can achieve a temperature that is 35.5 °C cooler than the hot structure. It should be noted that many commercial coating and paint materials already have intrinsic thermal emission features [36]. Therefore, researchers are encouraged to compare the performance of recently investigated materials with commercial products to claim the actual enhancement.

C. Photonic crystals

Photonic crystals (PhCs) or photonic bandgap (PBG) materials refer to materials that consist of periodically changed refractive indices introduced by micro/nanostructures in either one dimension (1D), two dimensions (2D), or three dimensions [108]. Most of these materials show complete PBGs, therefore allowing selective reflection or transmission of photons at discrete frequencies [Fig. 4(a)] [109]. By scaling this frequency selection to the thermal wavelength regime, PhC structures have attracted renewed interest in radiative cooling [14,105–124]. For example, Zhu *et al.* [105] experimentally demonstrated a periodic silica square lattice, as shown in Fig. 4(b). Due to the intrinsic transparency of silica in the VIS range and strong thermal emission in the MIR range, the obtained PhC structure not only allowed sunlight to travel through without introducing a heating effect but also enabled an efficient radiative cooling effect. Following this strategy, this same group reported another 2D PhC using a combined structure of periodic quartz/Si_3N_4 squares integrated on top of a multilayered reflector [Fig. 4(c)] [110]. Different from the structure shown in Fig. 4(b), this structure exhibited broadband reflection through the entire solar spectrum range and narrowband thermal emission only within the atmospheric

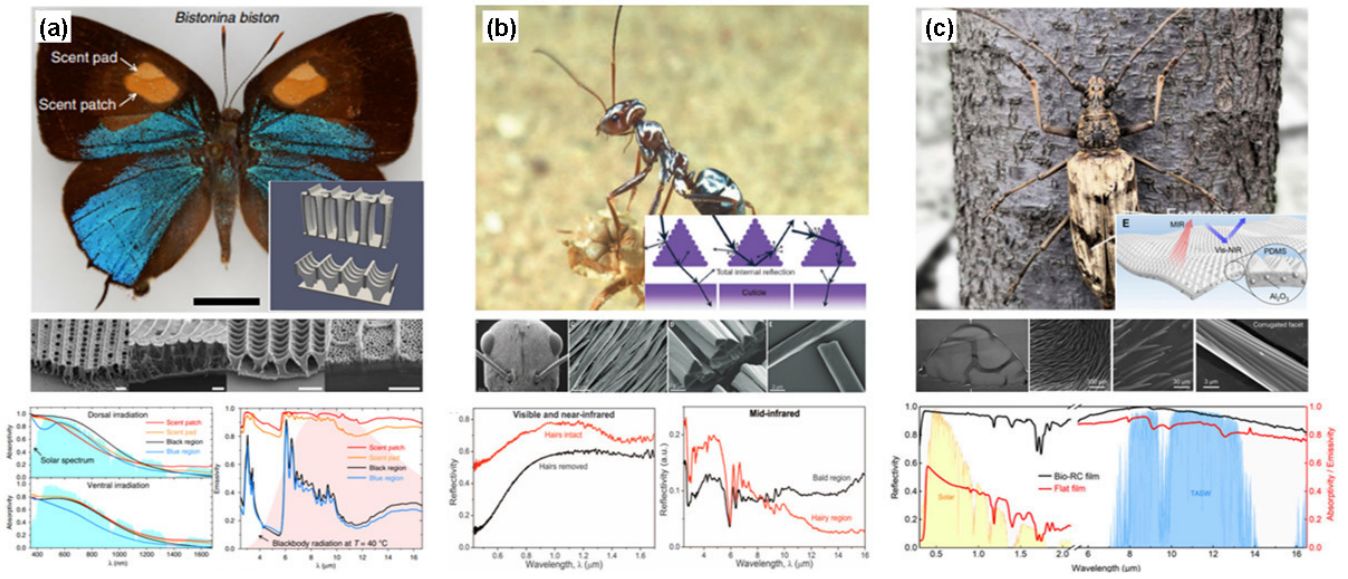

FIG. 5. (a) Separate areas in the wings of butterflies show different surface morphology and optical spectra. Copyright 2020 Springer Nature (Ref. [103]). (b) The hair on silver ants shows triangular microstructures, resulting in a silvery appearance and high thermal emissions. Copyright 2015 American Association for the Advancement of Science (Ref. [104]). (c) The skin of the *Neocerambyx gigas* beetle is composed of multiple micro/nanostructures, which shows high reflectivity in the visible (VIS)-near infrared (NIR) range and high emissivity in the midinfrared (MIR) range. Copyright 2020 National Academy of Sciences (Ref. [130]).

transparency windows of 8–13 μm and 17–25 μm, which was optimized for subambient radiative cooling. As a result, this proposed structure achieved a net cooling power of $>$ 100 $\mathrm{W/m^2}$ even under direct solar illumination.

PhCs have also been fabricated using self-assembled opals, as shown in Fig. 4(d). Unlike most rigid photonic structures, a self-assembled opal emitter is flexible and scalable [125,126], which is attractive for many radiative cooling applications. For example, Lin *et al.* [76] reported a monolayer of closely packed silica microspheres coated on a silicon oxynitride (SiO_xN_y) layer and Ag substrate [Fig. 4(e)]. This structure shows a high solar reflectance of 96.4%, while achieving a narrowband emissivity only within the 8–13 μm range. Kim *et al.* [111] also proposed a close-packed silica opal structure with uniform diameters on a silicon wafer [Fig. 4(f)]. The obtained structure shows minimized solar absorption, while the intrinsic thermal emission of SiO_2 enables a strong cooling effect. Intriguingly, the Bragg diffraction generated by the periodic SiO_2 array produces a variety of colors depending on the diameter of the opal. Compared with traditional dyes and pigments, these structural color strategies are particularly appealing to integrating radiative cooling with colorful coatings due to their minimized solar absorption.

D. Biomimetic structures

Micro/nanostructures for thermal regulation have been used by animals, plants, and insects for millions of years [103,104,127–134]. For instance, polar bears have evolved to have fur hairs with hollow cores in a multitude of sizes [127]. Not only will the hierarchical hollow structure provide effective thermal insulation to minimize heat loss, but it also suppresses thermal emission losses from the skin. Another example of biological structures for thermal management are the wings of butterflies [103,129], which are covered with nanopillars or nanorods and result in vivid colorful appearances (having been reported over a decade ago [129]). Recent measured results show that the wings of butterflies exhibit various emissivity in different areas due to the varied surface morphologies, which allow butterflies to regulate their body temperature via thermal radiation [Fig. 5(a)] [103]. By studying these natural species, researchers developed biomimetic structures to enable efficient thermal management. For example, Shi *et al.* [104] analyzed the skin structures of silver ants in the African desert [Fig. 5(b)]. The modeling results show that the triangular hair arrays with flat bottoms and corrugated facets exhibit high reflection in the VIS and NIR ranges while retaining high emissivity in the MIR range. Additionally, Zhang *et al.* [130] developed a micropyramid-arrayed polymer matrix with random ceramic particles inspired by the *Neocerambyx gigas* beetle [Fig. 5(c)]. Due to both the internal reflection from the pyramid structure and Mie scattering from the alumina particles, the obtained structure shows a high solar reflection of 95%. As a result, this structure enables an effective cooling power of $\sim$90.8 $\mathrm{W/m^2}$ and a passive temperature reduction of up to 5.1 °C under direct sunlight. Additionally, natural materials were engineered to realize daytime radiative cooling. For example, Li *et al.* [71] reported a delignified natural wood for daytime radiative cooling. In their study, multiscale cellulose nanofibers were engineered to be highly scattering in the VIS range, with a low solar absorption of only 4%, but strongly emissive in the 8–13 μm window over a broad angular range. Similarly, Zhou *et al.* [135] demonstrated a transparent bamboo, which consisted of a densely packed structure filled with pores of varying size, fabricated via the delignification of natural bamboo and subsequent epoxy infiltration. Compared with its opaque natural bamboo counterpart, transparent bamboo has high transmittance in the

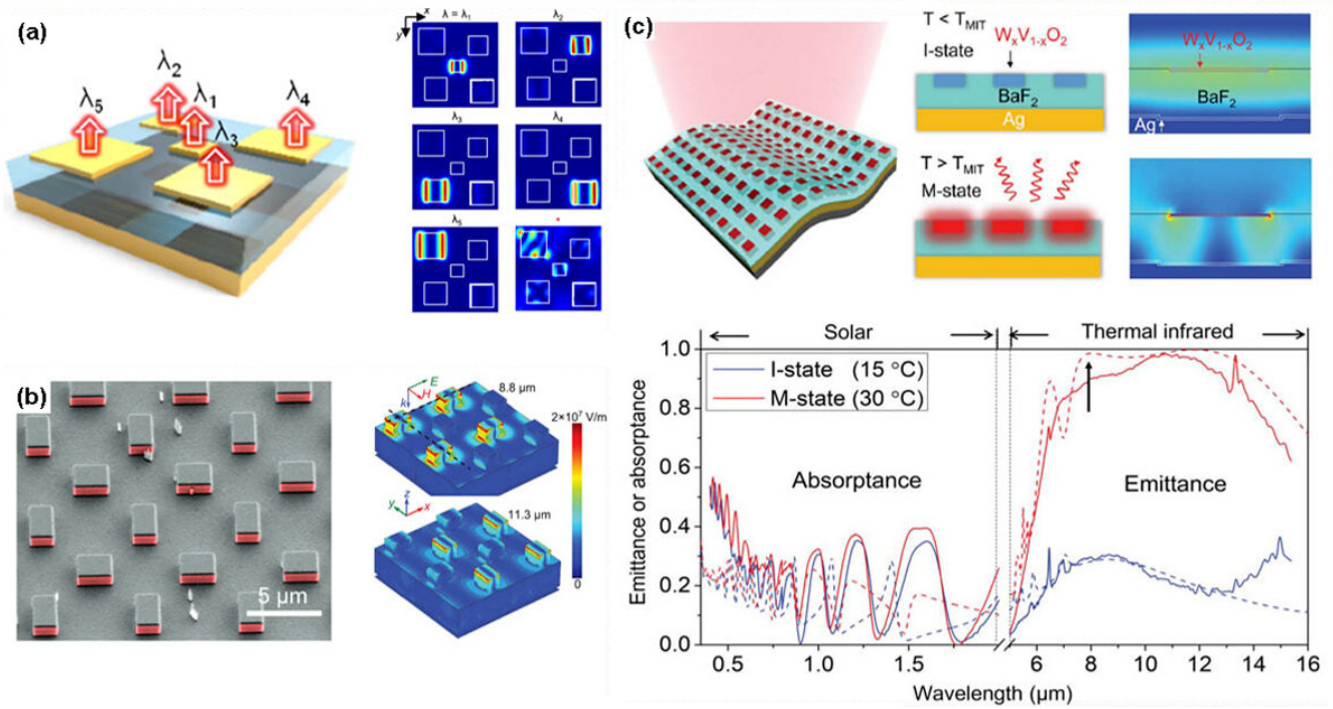

FIG. 6. (a) A square-lattice metasurface with five differently sized copper patterns. Copyright 2021 American Chemical Society (Ref. [140]). (b) A metasurface consisting of Ag-loaded, *n*-doped silicon resonators. Copyright 2017 Wiley (Ref. [141]). (c) A tungsten-doped VO_2 metasurface that realizes contrary midinfrared (MIR) emissivity at different modes. Copyright 2021 American Association for the Advancement of Science (Ref. [65]).

VIS range and near unity emission in the MIR range, enabling a strong radiative cooling effect.

E. Metasurfaces

Typical metasurfaces are planar surfaces with morphological structures that produce strong light-matter interactions at subwavelength scales [136]. Due to the magnetic resonances produced by nano/microstructures, the absorption or emission peaks can be tuned from VIS to MIR [137]. By engineering the geometries of nano/microstructures, metasurfaces have been widely used for applications such as metalenses [138] and holography [139]. In recent years, metasurfaces also have been engineered to perform the task of radiative cooling [33,118,140–149]. The structures developed in these studies are normally composed of two parts: (1) a top dielectric resonator or cavity, which is normally transparent within solar wavelengths, and emissive in the infrared range, and (2) a metal reflector [e.g., Ag or aluminum (Al)], which minimizes the solar heat gain. For example, Cho *et al.* [140] reported a square-lattice array with five differently sized copper patterns [Fig. 6(a)]. Due to the resonance derived from the gap plasmon cavity, the structure exhibits tunable absorption peaks in the MIR range. Additionally, by fabricating many different sized patterns on the surface, they demonstrated broadband thermal radiation within the 8–13 μm range, which was essential for subambient radiative cooling. Another example of a metasurface-based radiative cooler consisted of Ag-loaded, *n*-doped silicon resonators, as shown in Fig. 6(b) [141]. Due to the strong magnetic dipole resonance supported by the dielectric resonator, the structure exhibits strong, wide-angle emissivity that matches the main atmospheric transparency window of 8–13 μm. Their modeling results show that this proposed metasurface can achieve a temperature reduction of 11.14 °C during the nighttime and 8.25 °C during the daytime. Furthermore, tunable thermal regulation can be realized by introducing phase transition materials. For example, vanadium dioxide (VO_2) experiences a phase change from the metal to the semiconductor phase when its transition temperature of 67 °C is reached, followed by a significant change in its refractive index [65,146–149]. However, VO_2 thin films normally have small differences in MIR emissivity between the two phases, which constrains its feasibility in radiative cooling. Recently, this challenge was addressed by incorporating thin films of VO_2 with a metasurface. As shown in Fig. 6(c), Tang *et al.* [65] developed a mesh structure composed of thin tungsten-doped VO_2 nanopatterns on a barium fluoride substrate. Their results demonstrated that the MIR thermal emissivity of the structure increased from 0.2 to 0.9 when the surface temperature reached 22 °C. As a result, it showed a suppressed thermal emission in cold environments and strong thermal emission in warm environments, enabling distinct thermal regulating modes under different weather conditions.

F. Porous polymers

As previously discussed in Sec. II, many polymer materials exhibit strong thermal emission within the atmospheric window range, which is desirable for radiative cooling applications. However, the intrinsic absorption of polymers in the UV and NIR ranges reduces the cooling power under solar illumination, which requires further structural optimization.

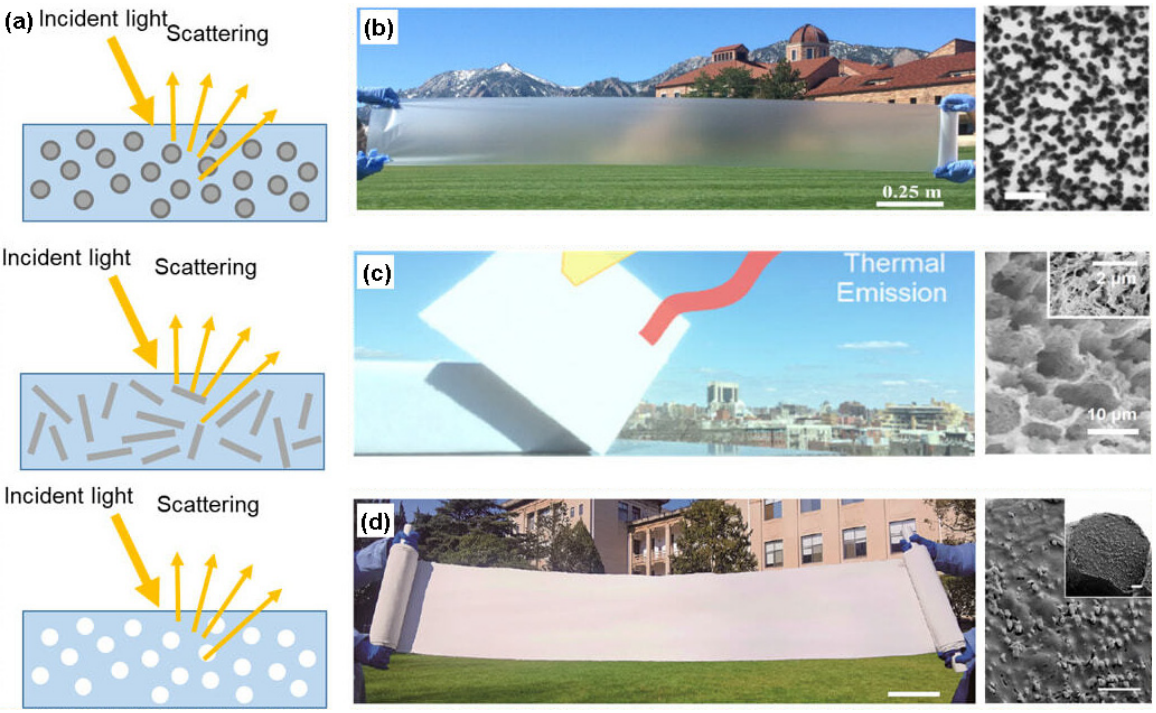

FIG. 7. (a) Schematic of Mie scattering introduced by micro/nanoparticles, fibers, and air voids. (b) Photo and scanning electron microscopy (SEM) image of SiO_2 microsphere embedded TPX thin film. The scale bar is 40 μm in the right image. Copyright 2016 American Association for the Advancement of Science (Ref. [42]). (c) Photo and SEM image of hierarchical porous PVDF thin film. Scale bar is 10 μm in the right image and 2 μm in the inset. Copyright 2018 American Association for the Advancement of Science (Ref. [64]). (d) Photo and SEM image of hierarchical polymer thin film. Scale bar is 20 cm in the left photo and 5 μm in the right image. Copyright 2021 American Association for the Advancement of Science (Ref. [72]).

To address this challenge, researchers have combined polymer thin films with disordered particles, fibers, or air voids [Fig. 7(a)] [38,134,150–173]. These randomly distributed light scatterers are within the range of nanometers to micrometers in size, which enables a strong Mie scattering effect or diffusive reflection effect. Interestingly, some of these hybrid materials also exhibit stronger IR emissions due to the phonon-enhanced Fröhlich resonance [42]. For example, Zhai *et al.* [42] demonstrated a high-performance cooling sheet by embedding polymethylpentene (TPX) thin film with SiO_2 microspheres [Fig. 7(b)]. The obtained thin film shows an average thermal emission of 0.93 in the LWIR range. Moreover, due to the Mie scattering introduced by the microsized SiO_2 particles and high reflection from the Ag back reflector, the solar absorption of this thin film emitter is <4%, resulting in a cooling power of 93 W/m^2 under direct sunlight. This strong scattering effect can also be achieved by replacing the nano/microparticles with air voids. For instance, Mandal *et al.* [64] reported a hierarchical porous poly(vinylidene fluoride-co-hexafluoropropene) (PVDF) thin film using a simple phase-separation process [Fig. 7(c)]. Due to the abundant air voids with sizes ranging from nanometers to micrometers, the obtained coating exhibits a strong solar reflectance of 0.96 and a strong thermal emission of 0.97. One can also obtain a broader solar reflection by combining dielectric nanoparticles with air voids. For instance, a multilayer metafabric was reported with ultrabroadband reflection that covers the entire UV-VIS-NIR range, which consists of polylactic (PLA) embedded with TiO_2 particles and porous polytetrafluoroethylene (PTFE) [Fig. 7(d)] [72]. Moreover, due to the intrinsic thermal emission from both the PTFE and PLA, the white sheet exhibits a broadband thermal emissivity from 4 to 24 μm. This excellent spectral selectivity renders high cooling performance and can be developed into a wearable fabric, as will be discussed in Sec. V B.

It should be noted that porous structures can also be utilized as thermally insulating materials [171–173]. For example, the aforementioned cooling wood is a typical thermally insulating material [71]. This combination of radiative cooling with high thermal resistance can minimize the heat exchange with the warmer environment while simultaneously dissipating latent heat via thermal radiation. In cold seasons when cooling is undesired, a thermally insulating material also minimizes the heat loss from the interior space. This is highly desired for building thermal management applications, as illustrated in Fig. 8(a) [173]. Authors of many other studies also developed cooling materials with low thermal conductivity [Figs. 8(b) and 8(c)] [71,171–173]. For example, Zhou *et al.* [172] fabricated a porous polydimethylsiloxane (PDMS) using a sugar template and realized a thermal conductivity of 0.06 $W\,m^{-1}\,K^{-1}$. Zhong *et al.* [171] developed a hollow PVDF microfiber material with an even lower thermal conductivity of 0.014 $W\,m^{-1}\,K^{-1}$. More recently, Yue *et al.* [173] fabricated an aerogel using wastepaper and reported thermal conductivity of 0.028 $W\,m^{-1}\,K^{-1}$. Their modeling results show that a thermally insulating radiative cooler outperforms both radiative cooling-only materials and thermal insulation-only materials in cooling energy saving, which is particularly

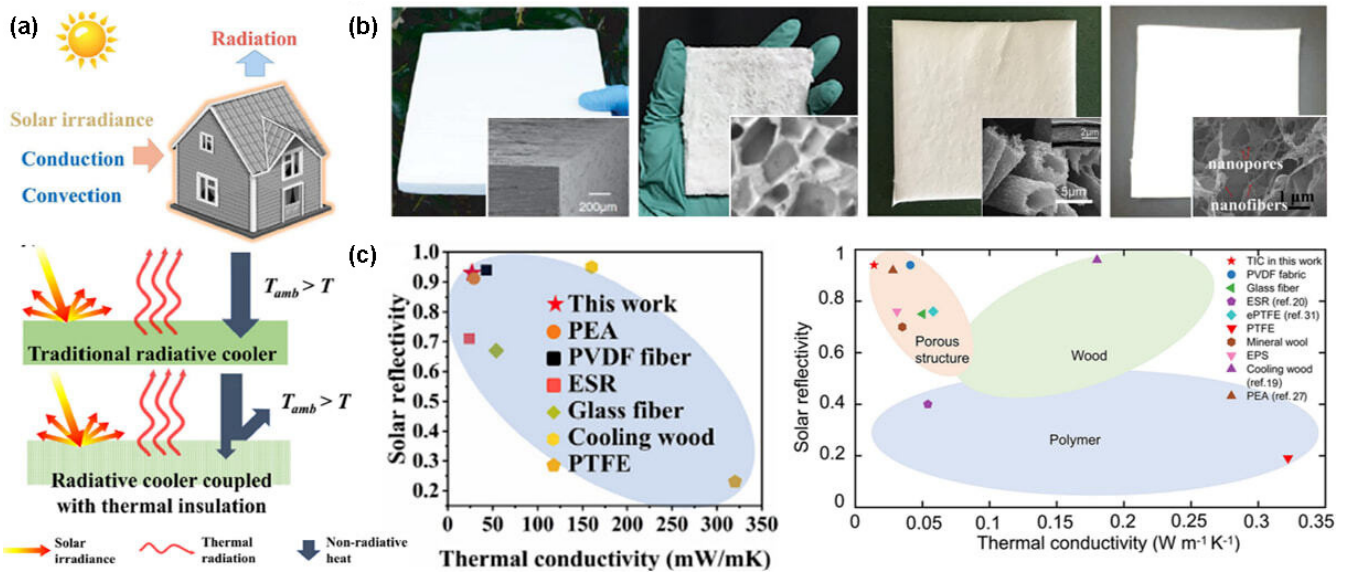

FIG. 8. (a) Schematic of the heat exchange on a traditional radiative cooler and thermally insulating radiative cooler. Copyright 2021 American Association for the Advancement of Science (Ref. [173]). (b) Photos and scanning electron microscopy (SEM) images of thermally insulating radiative coolers in recent studies. From left to right, the photos show cooling wood [71], porous PDMS [172], hollow microfiber cloth [171], and cooling aerogel [173]. (c) Summarized thermal conductivity of different radiative cooling materials in recent studies. (b) and (c) are reproduced with permission from 2019 American Association for the Advancement of Science (Ref. [71]), 2021 Wiley (Ref. [172]), 2021 American Chemical Society (Ref. [171]), and 2022 Elsevier (Ref. [173]).

attractive for building thermal regulation. Nevertheless, when compared with the state-of-the-art radiative coolers, the actual merit of thermally insulated radiative cooling remains unclear with respect to energy savings and requires further research and investigation.

G. Paints and pigments

Painting materials are also promising candidates for large-scale radiative cooling due to the strong Mie scattering introduced by dielectric particles [174–178]. By introducing micro/nanospheres with wavelength-scale dimensions into polymer binders, the obtained structure can strongly scatter the incident sunlight and realize a minimized solar absorption. It was reported that dielectric particles with high refractive indices, such as hexagonal boron nitride, are preferred, as the large dielectric contrast permits a stronger scattering effect [112]. More importantly, unlike previously discussed polymer thin films, paints can be directly applied on complex textured surfaces [36], which is particularly attractive for applications like building envelopes. However, the solar reflectance of conventional white paints (mainly composed of SiO_2 and TiO_2 particles) is normally not strong enough for subambient radiative cooling [39,40], especially in UV and NIR range. Motivated by this challenge, recent researchers have developed cooling paints for more efficient thermal regulation. For example, Li *et al.* [39,40] reported cooling paints with ultrahigh solar reflectance, as shown in Figs. 9(a) and 9(b). Compared with the TiO_2-based white paints, these proposed cooling paints showed higher reflection in the UV and NIR ranges due to the large bandgap pigments (e.g., $BaSO_4$ and $CaCO_3$) mixed in the acrylic slurry. Similarly, Xue *et al.* [75] also proposed cooling paint by introducing extra fluorescent microparticles in conventional paints [Fig. 9(c)]. Not only did the SiO_2 and TiO_2 particles induce strong Mie scattering within the solar wavelength range, the Purcell effect introduced by the fluorescent particles also converted part of the absorbed solar irradiance to visible light emission. Consequently, the obtained paint showed a reduced solar heating effect, which was beneficial for daytime radiative cooling. Importantly, these white paints can be combined with colorful dyes or pigments to meet aesthetic purposes. Although the pigments in conventional colored paintings inevitably introduce a strong solar heating effect, the overall solar absorbance can be minimized by controlling the thickness of the colored layer. As shown in Fig. 9(d), by coating a thin colored layer on a white PVDF painting, the obtained structure not only showed identical pink color to a commercial paint but also showed improved NIR reflection (from 0.1 to 0.51) [174]. As a result, the proposed bilayer coatings showed a reduced temperature that is 3 to 15.6 °C lower than commercial paintings with identical colors.

IV. SYSTEM DESIGN

In a pioneering work, Raman *et al.* [13] characterized the cooling power of their proposed radiative cooler using an electric heater. By measuring the heating power that was required to maintain the cooler at ambient temperature, they could obtain the actual cooling power of the emitter. This design was further improved by adding a feedback-controlled electric heater to monitor the cooling power in real time [42]. However, according to Sec. II, the net cooling power of an emitter P_{net} will be affected by the weather conditions, such as solar irradiance, wind, cloud, and relative humidity. To suppress these weather effects, a thermally insulated container

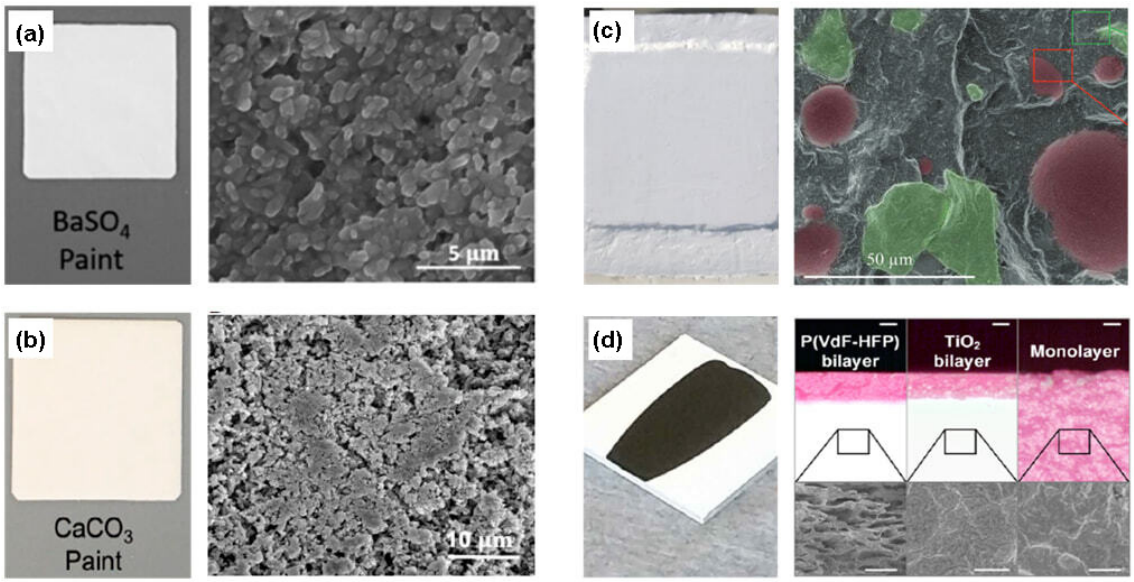

FIG. 9. (a) Photo and scanning electron microscopy (SEM) image of $BaSO_4$ cooling paint. Copyright 2021 American Chemical Society (Ref. [40]). (b) Photo and SEM image of $CaCO_3$ cooling paint. Copyright 2020 Cell Press (Ref. [39]). (c) Photo and SEM image of ecofriendly cooling paint with fluorescent microparticles. Copyright 2020 Wiley (Ref. [75]). (d) Photo and SEM image of PVDF bilayer colored paint. Copyright 2020 American Association for the Advancement of Science (Ref. [174]).

sealed by PE film is normally implemented, as shown in Fig. 10(a). Based on this design, many other cooling systems were designed to realize improved cooling performance by maximizing P_{rad} and/or minimizing P_{sun}, P_{atm}, and P_{nonrad} [31,44,66,68,179–181]. Here, we will summarize these considerations in system design.

A. Minimized absorbed solar absorption (P_{sun})

Considering the solar incident power of 1000 W/m^2, the optical absorption of a thermal emitter should be $<10\%$ to obtain subambient cooling effect during the daytime. Therefore, most radiative emitters are white in color (e.g., Refs. [64,65]). On the other hand, the incident solar heating effect can also be reduced using planar sunshades, which are normally made of broadband reflective metals such as Ag or Al [31,44,66,80]. However, a vertical planar sunshade is usually insufficient due to the changing solar incident angles [44]. To address this issue, Zhou *et al.* [44] reported a V-shaped solar shelter and realized all-day radiative cooling, as shown in Fig. 10(b). The solar shelter was made of a spectrally selective material, which was highly absorptive in the VIS-NIR range and reflective in the MIR range. When placed on top of a sky-facing emitter, the solar shelter absorbed the incoming solar irradiance while directing the thermal radiation from the thermal emitter to the sky. Another example is a solar tracking system that can actively adjust the position of an Al reflector to block direct solar illumination to the emitter [Fig. 10(c)] [66]. In this system, a double-layered nanoporous PE was also used to further reduce P_{sun}. Despite the complexity, this solar-tracking system was also useful for thermal regulation in concentrated PV systems [184].

B. Minimized absorbed atmospheric radiation (P_{atm})

As discussed in Sec. II, the atmospheric transmission is dependent on both humidity and zenith angle. As a result, the absorbed atmospheric radiation P_{atm} is significantly higher in humid areas than arid areas, especially at large zenith angle. By considering the angular-dependent atmospheric transmission shown in Sec. II B, one can reduce the P_{atm} by coupling thermal radiation into a smaller zenith angle range where the atmosphere has higher transmittance. For example, the Al corn mirror shown in Fig. 10(d) realized an improved cooling performance in a humid environment and resulted in an elongated dewing period by 2.5 h [85]. Intriguingly, such tapered guides also improve the cooling performance in a complex environment. As revealed by Zhou *et al.* [44], a radiative emitter reduced the temperature by ~11 °C when tested in a parking lot, whereas it only achieved a temperature reduction of 2 °C when tested in crowded urban settings. By implementing a spectral selective V-shaped solar shelter (a typical Al-based ceramic solar absorber [84]) shown in Fig. 10(b) (also known as a tapered guide), not only was the sunlight blocked, but also the thermal emission was coupled to a narrower zenith angular range. This approach is particularly attractive to address the cooling demand in urban areas [184].

C. Minimized parasitic heat (P_{nonrad})

Nonradiative heat transfer (P_{nonrad}) is one of the major factors that affects temperature reduction, especially when the temperature difference between the emitter and ambient air is large [31]. Although a low-density PE is normally used to suppress the air convection, it is vulnerable and will degrade over time [179]. Additionally, a single PE film is too thin to provide sufficient thermal insulation, limiting the net cooling capability [179]. Therefore, researchers developed advanced

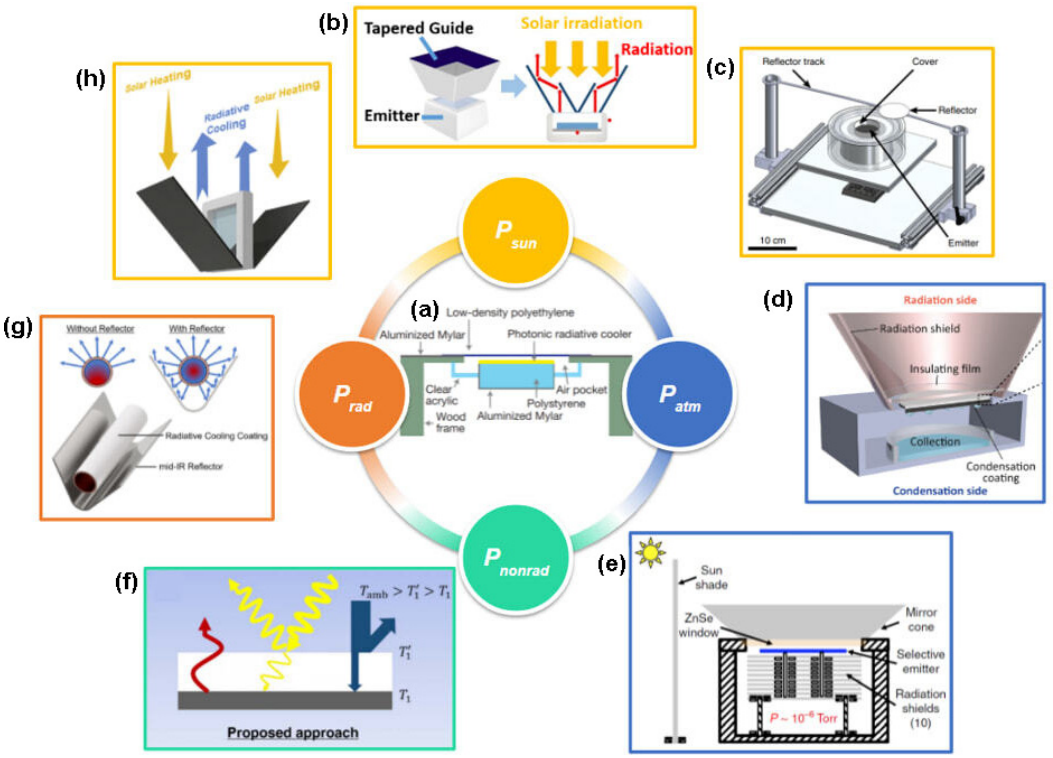

FIG. 10. Schematic of the system designs in recent radiative cooling research. (a) The rooftop measurement apparatus reported in the first subambient daytime radiative cooling research. Copyright Springer Nature 2014 (Ref. [13]). (b) The tapered guide for optimized daytime cooling in urban settings. Copyright 2019 Springer Nature (Ref. [44]). (c) A radiative cooling design with a solar-tracked shelter for minimized solar absorption. Copyright 2018 Springer Nature (Ref. [66]). (d) A radiative cooling design with a radiation shield for reduced atmospheric radiation. Copyright 2021 American Association for the Advancement of Science (Ref. [85]). (e) A vacuum chamber that enables an ultralow temperature reduction under solar illumination. Copyright 2016 Springer Nature (Ref. [31]). (f) The PE aerogel for minimized nonradiative heat transfer and solar absorption. Copyright 2019 American Association for the Advancement of Science (Ref. [68]). (g) The concentrated radiative cooling system that realized the enhanced localized cooling power on the cooling pipe. Copyright 2022 Elsevier (Ref. [181]). (h) The double-sided radiative cooling system with spectrally selective mirrors, realizing radiative cooling and solar heating simultaneously. Copyright 2021 Cell press (Ref. [180]).

materials or systems to replace transparent PE films and realized minimized P_{nonrad} [31,67,68]. For example, Chen *et al.* [31] designed a vacuum system and explored the limit of temperature reduction [Fig. 10(e)]. In this system, a zinc selenide window was employed to replace the thin PE film due to its high MIR transmittance and strong mechanical strength. As a result, a superior temperature reduction of 42 °C below ambient was realized when the vacuum of the thermal isolating container reached 10^{-5} Torr. A more practical method is to use an opaque porous PE aerogel, which showed extremely low thermal conductivity (e.g., 0.028 $\text{W m}^{-1}\text{ K}^{-1}$) as reported by Ref. [68]) and realized minimized P_{nonrad} and P_{sun} simultaneously [Fig. 10(f)]. Moreover, the intrinsic transparency of PE in the MIR range ensured efficient transfer of thermal radiation to the sky. With this PE aerogel, a temperature reduction of 13 °C was demonstrated, representing one of the best cooling results under standard atmospheric conditions.

D. Maximized localized cooling power density

In most of the aforementioned radiative cooling systems, the thermal emitter is placed horizontally to ensure full access to the sky. In such a case, only the top surface has access to the sky, while the bottom surface contributes little to the radiative heat transfer. Therefore, the cooling power limit is $\sim$160 W/m^2 at 300 K [14–21]. In addition, most planar radiative cooling systems do not harvest solar energy to minimize P_{sun}. On the other hand, with a carefully designed system, one can enhance the cooling power further by coupling the thermal radiation from both surfaces of the cooler to the sky. Simultaneously, the incident solar energy can also be collected rather than scattered. For example, Zhou *et al.* [180] designed a double-sided system that incorporated thermal radiation from both surfaces of a vertically aligned thermal emitter to the sky [Fig. 10(h)]. To minimize the absorbed solar power while ensuring efficient radiation heat transfer between the emitter and the sky, two spectrally selective mirrors (a graded nanocomposite material fabricated using a cosputtering technique) were employed. Their results showed that this double-sided system enabled a localized cooling power of $\sim$270 W/m^2 and a temperature reduction of 14 °C, which was a significant improvement compared with regular single-sided sky facing systems. Furthermore, since the mirrors are also absorptive in the solar wavelength range, this double-sided system can harvest solar energy simultaneously. On a regular sunny day, the two-mirror temperature reached 55 °C, representing a hybrid radiative cooling and solar heating system. Similarly, Peoples *et al.* [181] nested a cooling pipe with $BaSO_4$ cooling

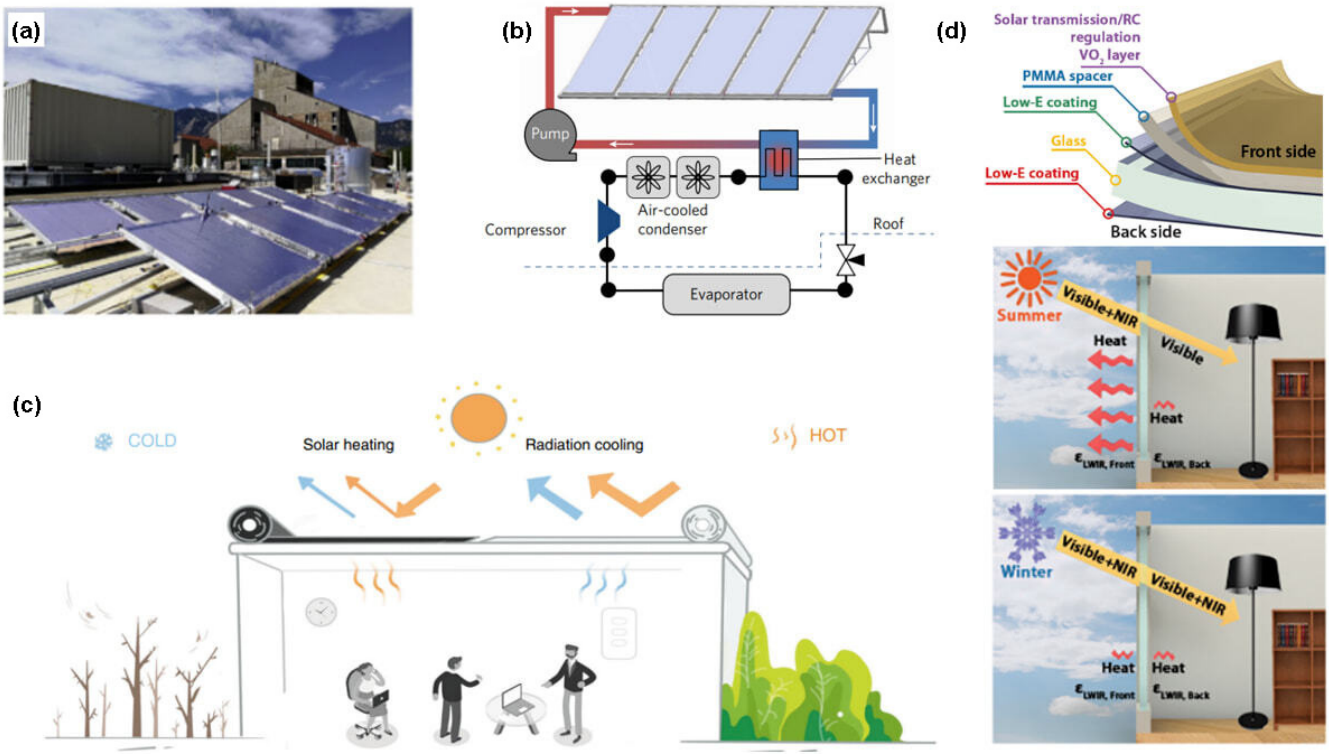

FIG. 11. (a) A photo illustrating radiative cooling panels being implemented on buildings. Copyright 2019 Cell Press (Ref. [73]). (b) A schematic of radiative cooling panels integrated with traditional condensers. Copyright 2017 Springer Nature (Ref. [183]). (c) A schematic of a switchable passive cooling/heating system for interior space thermal management. Copyright 2020 Springer Nature (Ref. [195]). (d) A VO_2 based smart window that can dynamically regulate the interior temperature depending on the weather conditions. Copyright 2021 American Association for the Advancement of Science (Ref. [72]).

coating in an Al trough, as shown in Fig. 10(g). Owing to the high MIR reflection of the trough, thermal radiation from both the top and bottom of the pipe were coupled to the sky and contributed to the radiative cooling. Compared with a pipe without a trough, the temperature reduction obtained by this concentrated cooling design was improved by a factor of two. These versatile systems are particularly attractive for sustainable applications and energy harvesting, as discussed in the next section.

V. APPLICATIONS

Building upon the spectral selective features of radiative cooling materials, various applications can be developed by considering specific requirements, such as compatibility, durability, wearability, etc. In this section, we will summarize major applications by integrating radiative cooling features.

A. Building

It is believed that radiative cooling can save electricity consumption from cooling the building due to its passive nature [84,167,182–203]. The polymers and paints discussed in Sec. III are ideal because they can be directly applied to the exterior surface of building envelops and roofs [39,40,64,75,174]. For example, cooling paints shown in Fig. 9 can strongly adhere to metal and concrete substrates [39,40,75,174]. The PVDF coating shown in Fig. 7(c) also has excellent compatibility with copper, plastic, and wood substrates [64]. Of course, these cooling paints can be coated using simple and inexpensive processes like dip coating and spray coating over large scales. Additionally, by considering thermal properties such as thermal conductivity and heat capacity, these cooling paints can also be integrated with conventional heating, ventilation, and air conditioning (HVAC) components [73,183] or as thermal storage materials [203]. For example, a cooling panel consisting of a thin radiative cooling film laminated on the water container was used to cool the condenser in an air conditioner unit [Fig. 11(a)] [73]. With a size of 13.5 m^2, the proposed system could provide a maximum cooling power of 1296 W at night and an average cooling power of 607 W at noon. Another work was also reported for building thermal management, where the produced cold water was utilized to remove heat from the condenser [Fig. 11(b)] [183]. By running the coolant at a flow rate of 0.2 L min^{-1} m^{-2}, the proposed radiative cooling panel could reduce the condenser temperature below the air temperature by 5 °C. It was estimated that 21% of the electricity used for building cooling in an arid climate could be saved by implementing this system.

However, one major challenge for these building envelope applications is the fouling issue [36], e.g., the accumulation of dust on exterior surfaces. To address this practical challenge, superhydrophobic surfaces have been reported to realize self-cleaning functionality for long-term radiative cooling [155,167,196–202]. Another challenge is the stability

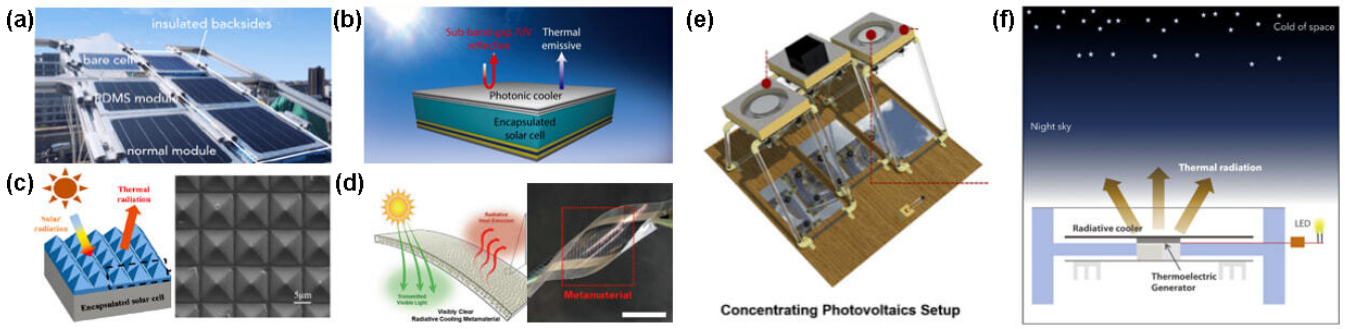

FIG. 12. (a) A photo of the field test for planar PDMS coating on encapsulated PV modules. Copyright 2021 Wiley (Ref. [70]). (b) Schematic of a multilayer dielectric photonic structure for solar cell radiative cooling. Copyright 2017 American Chemical Society (Ref. [213]). (c) Schematic of a periodic pyramid PDMS coating for solar cell radiative cooling. Copyright 2021 Elsevier (Ref. [215]). (d) Schematic and photo showing a flexible metamaterial for PV cell cooling. Copyright 2022 Wiley (Ref. [221]). (e) Schematic of a reverse design for concentrated photovoltaic cooling. Copyright 2020 Cell Press (Ref. [69]). (f) Nighttime power generation enabled by radiative cooling. Copyright 2019 Cell Press (Ref. [83]).

of the materials under harsh environments, such as long-term UV exposure, high temperature, and high humidity. Additionally, considering the seasonally dependent cooling demand, dynamic thermal regulation is also desired. Researchers designed switchable radiative cooling systems that can provide either cooling or heating depending on the weather conditions [72,74,165,180,189–195]. For example, a switchable system equipped with rotary actuators [Fig. 11(c)] could selectively expose its solar heating surface (zinc film with copper particle) or radiative cooling surface (PDMS thin film on Ag reflector) [195]. These switchable modes can also be realized by a smart window composed of VO_2 thin films. As shown in Fig. 11(d), when the VO_2 is coated on indium tin oxide multilayers, the smart window can selectively transmit the sunlight in cold weather while blocking sunlight in warm weather, especially within the NIR range [72]. Remarkably, this smart window also showed switchable thermal transmissivity, enabling season-dependent thermal regulation: (1) over the summertime, the high MIR emissivity (0.61) realized cooling by releasing the heat from interior space to the sky, whereas (2) in winter, the low MIR emissivity (0.21) corresponds to the heating mode by suppressing the radiation heat transfer. These designs are particularly attractive to address the energy crisis raised by the thermoregulation [194].

B. Semiconductor devices

Thermal management is one of the major challenges for semiconductor devices. Efficiency and lifetime of semiconductor devices (e.g., PV cells [204], LEDs [205], and laser diodes [206]) are most sensitive to their operating temperature. For example, it was estimated that every 1 °C temperature increase in crystalline silicon PV modules would lead to a relative efficiency decline of 0.45% [105]. Mainstream cooling strategies include forced-air cooling, thermoelectric cooling, and water cooling, all of which tend to be energy hungry. In contrast, radiative cooling shows great potential to cool semiconductor devices with no additional electricity consumption Ref. [207–211]. For example, the broadband photonic structure shown in Fig. 4(b) has been implemented to reduce the operating temperature of silicon solar absorbers [105]. However, it should be noted that encapsulating layers of commercial solar cells, such as glass, ethylene-vinyl acetate and Tedlar backsheets, already show high thermal emissivity for radiative cooling [70]. According to a recent combined theoretical and experimental analysis, a broadband PDMS emitter can only reduce the temperature of a commercial PV module [Fig. 12(a)] by <1 °C, corresponding to a relative efficiency improvement of $\sim$0.38% [70]. This limitation of radiative cooling in commercial PV modules can be partially addressed by applying a coating with optimized spectra [133,212–218]. For example, Li *et al.* [213] designed a multilayer dielectric stack of Al_2O_3/SiN/TiO_2/SiN [Fig. 12(b)] to suppress the solar heating effect by realizing strong reflectivity in both UV and 1.3–1.8 μm wavelength ranges. Simultaneously, this multilayer also exhibits high emissivity over a broad wavelength range from 4–25 μm. By applying this cooling coating to an encapsulated solar cell module, the temperature of the module was lowered by 5.7 °C. Furthermore, radiative cooling performance can also be improved by optimizing the angular emissivity. It was revealed that the thermal emission of the encapsulation layer of commercial PV modules (e.g., glass) will be significantly at an emission angle over 60°, hence limiting the cooling power [28]. To address this issue, Wang *et al.* [215] developed a pyramid PDMS PhC coating that showed over 90% transmittance in the VIS range and near unity emissivity in MIR range across a large angle range [Fig. 12(c)]. As a result, the operating temperature of the PV module was reduced by 2 °C compared with a commercial module.

Interestingly, radiative cooling strategies are also applicable to other PV devices [69,219–222]. For example, Lee *et al.* [221] developed a flexible and visibly transparent metamaterial for PV cells cooling, as shown in Fig. 12(d). The proposed material was made of silica aerogel microparticles in a silicone elastomer, showing 91% transmission in the VIS range and 98% emission in the atmospheric window range. This promising spectrum selectivity enables strong cooling effect and sunlight transmission, while the mechanical flexibility also allows it to be coated on flexible organic PV cells. Another example is for concentrated PV (CPV) module cooling [69]. By incorporating the thermal radiation from both

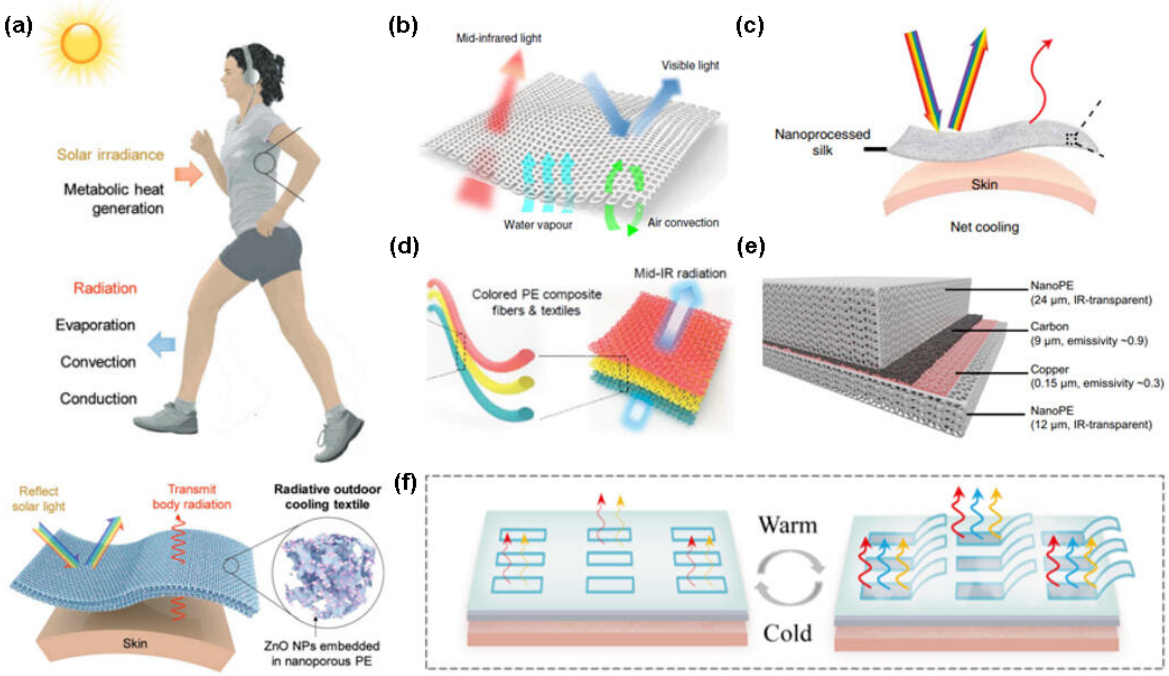

FIG. 13. (a) Schematic of a nanoporous PE cooling fabric embedded with ZnO nanoparticles. Copyright 2018 Wiley (Ref. [78]). (b) Schematic shows a knitted nanoPE fabric with cottonlike softness. Copyright 2018 Springer Nature (Ref. [231]). (c) Schematic of nanoprocessed silk embedded with Al_2O_3 nanoparticles. Copyright 2021 Springer Nature (Ref. [233]). (d) Schematic of colored PE textiles embedded with infrared (IR) transparent pigments. Copyright 2019 Cell Press (Ref. [77]). (e) Schematic of a dual-mode textile, in which the cooling side is composed of nanoPE/carbon, while the heating side is composed of nanoPE/copper. Copyright 2017 American Association for the Advancement of Science (Ref. [242]). (f) Schematic of a moisture responsive actuator for dynamic thermal regulation. Copyright 2021 American Association for the Advancement of Science (Ref. [243]).

the front and back sides of the panel to the sky [Fig. 12(e)], the operational temperature of a CPV was reduced by 10 °C with an open circuit voltage improved by 5.7%. More interestingly, a radiative cooling strategy was even integrated with the thermoelectric power generator (TEG) to demonstrate the concept of *antisolar cell* [83,223–230]. Opposite to regular solar cells harvesting solar energy during the daytime, a TEG device driven by radiative cooling can operate during both daytime and nighttime by emitting thermal energy to outer space. For example, a simple design composing of a black emitter coupled with a commercial TEG achieved a power generation of 25 mW/m^2 and drove a white LED at night [83] [Fig. 12(f)]. By modifying the system with spectrally selective emitters (i.e., emissive in 8–13 μm only) and considering state-of-the-art TEG devices, the power generation potential was estimated to be $> 2\,W/m^2$, much closer to the power generation limit of a Carnot engine (i.e., 6.4 W/m^2) [223]. This all-day operation is particularly attractive to off-grid applications, such as sensors and lighting in a dark environment.

C. Personal thermal management

Cloth is an essential tool to protect us from a variable environment. They are mostly made of fabrics that have excellent sweat permeability, which supports heat dissipation mostly via sweat evaporation [26]. However, due to colorful appearance, most fabric materials are absorptive in the solar wavelength range, which will inevitably introduce solar heating under direct sunlight illumination. Recently, researchers developed advanced textiles for personal thermal management [67,77,78,167,192,231–243]. In general, these studies can be classified into two categories. The first one is developing thermally transparent materials for cloth fabric. In this situation, the thermal emitter is the human skin. Its thermal radiation transmits through the cloth and can be dissipated via a radiative cooling channel. Typical examples of this type of research are based on nanoporous PE, which was featured as a promising cooling fabric due to its high solar reflectivity and MIR transmissivity [67]. Placed on top of human skin, a nanoporous PE film can scatter sunlight while allowing thermal radiation to be emitted. Such nanoporous PE films can be further optimized by embedding ZnO nanoparticles in the polymer fabric [Fig. 13(a)] [78]. Compared with normal textiles like cotton, these textiles realized a cooling effect of 5–13 °C on simulated skin. Peng *et al.* [231] also developed a large-scale knitted nanoPE fabric with cottonlike softness [Fig. 13(b)], showing a cooling effect of 2.3 °C on simulated skin. In addition to the thermally transparent material, the second category is a thermally emissive fabric [Fig. 13(c)]. In this category, the fabric functions as the emitter, where the heat is conductively transferred from the skin to the fabric [72,232,233]. For example, a nanoprocessed silk was reported for efficient personal thermal management. Owing to the embedded Al_2O_3 nanoparticles, the obtained cooling silk exhibited 90% emissivity in the 8–13 μm and 95% reflectivity within the solar spectrum range [233]. Under direct sunlight illumination, this cooling silk achieved a strong radiative cooling effect of 3.5 °C below ambient.

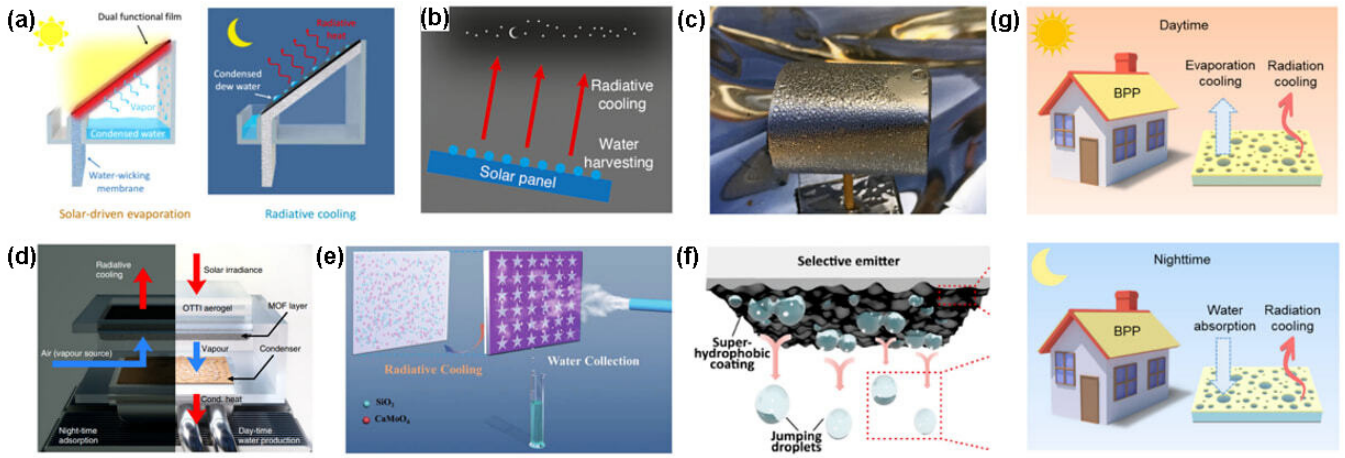

FIG. 14. (a) A dual functional system for all-day water harvesting. Copyright 2020 American Chemical Society (Ref. [249]). (b) A schematic show that a solar panel capable of harvesting water at night. Copyright 2020 American Chemical Society Ref. [63]. (c) A photo of a daytime water condensing device. Copyright 2019 National Academy of Science (Ref. [246]). (d) A schematic of an adsorption-based atmospheric water harvesting device assisted by radiative cooling. Copyright 2018 Springer Nature (Ref. [86]). (e) A schematic of a water harvesting surface with star-shaped hydrophilic patterns. Copyright 2020 Wiley (Ref. [247]). (f) A superhydrophobic carbon nanofiber coating on the back of a selective radiative emitter. Copyright 2021 American Association for the Advancement of Science (Ref. [85]). (g) A bilayer polymer that realizes synergetic cooling by evaporation and radiation. Copyright 2021 Elsevier (Ref. [157]).

The cooling textiles can be further combined with colorants for aesthetic purposes. As shown in Fig. 13(d), by mixing Prussian blue, iron oxide, or silicon particles in PE fibers, the proposed cooling textiles realized three different colors with minimized solar absorption in the NIR range [77]. Additionally, due to the MIR transparency of both the pigments and PE textile, the colored cooling textiles also exhibited ~80% transmissivity in the MIR range. When exposed to direct sunlight, the colored cooling textiles realized cooling effects of 1.6–1.8 °C lower than cotton. More interestingly, one can even realize dynamic thermal regulation using specially designed fabric to adapt to ambient temperature changes or seasonal meteorological variation [240–243]. As shown in Fig. 13(e), Hsu *et al.* [242] demonstrated a dual mode textile composed of nanoPE/carbon on the cooling side and nanoPE/copper on the heating side. By reversing the fabric, the textile either showed an emissivity of 0.8–1 on the cooling side or emissivity of 0.3 on the heating side, resulting in a cooling effect of 3.1 °C and a heating effect of 3.4 °C, respectively. This approach can be further optimized to be self-responsive using a nylon/metal heterostructure [243]. Depending on the environmental humidity, the flaps on the textile could open and close [Fig. 13(f)]. As a result, the closed textile realized heating mode by suppressing the radiative heat transfer between the skin and the environment, whereas the opened textile realized a cooling mode otherwise, revealing an application for personal thermal management [240].

D. Moisture harvesting

To address the severe challenge of water scarcity, an emerging topic is to develop materials and systems for atmospheric water harvesting [63,85,86,157,244–249]. However, the state-of-the-art water purification technology is constrained by the energy consumption required for heat dissipation [245]. It is also challenging to collect water in an environment with low relative humidity (for example, <60%) [86]. On the other hand, radiative cooling can achieve subambient cooling during both day and night, which is particularly attractive to facilitate moisture condensation. For example, Xu *et al.* [249] designed an all-day freshwater harvesting system [Fig. 14(a)] using natural nonradiative cooling during the daytime and radiative cooling at nighttime. This system achieved a water collection rate of $0.1\,\mathrm{L\,m^{-2}\,d^{-1}}$ at night when most commercial solar systems still cannot work. Similar results were also realized on solar panels [Fig. 14(b)], as most solar panels have a strong cooling effect at night that is not fully exploited [63]. Li *et al.* [63] demonstrated an average weekly water harvesting rate of $261\,\mathrm{mL/m^2}$ in Dubai. More interestingly, this water harvesting rate can be further improved by optimizing the optical properties of the radiative cooler. For example, Zhou *et al.* [246] demonstrated an all-day atmospheric water collector using a PDMS/metal emitter [Fig. 14(c)]. When placed under direct solar illumination, the collector strongly reflected sunlight and emitted thermal radiation, thus realizing a subambient cooling effect and enabling a water production rate that was twice that of a commercial condenser (e.g., model CRSQ-0.25 from the International Organization for Dew Utilization).

Furthermore, radiative cooling strategies can be utilized to enhance the water collection rate of other adsorption materials or surfaces [86,157,247,248]. As shown in Fig. 14(d), the radiative cooling film reduced the temperature of a metal-organic-framework (MOF)-based water collector by ~3 K, resulting in a 5–7% increase in the RH of the closed chamber [86]. As a result, a MOF-based atmospheric water collector was demonstrated that can operate in an exceptionally arid climate with RH of 10–40%. Additionally, by engineering the hydrophobicity of a radiative cooling surface, one can enhance the water harvesting rate. As shown in Fig. 14(e), star-shaped wettable patterns were fabricated on the backside of a PVDF radiative cooler [247]. Owing to the enhanced heat

dissipation enabled by radiative cooling, the obtained water collection rate was increased by 43–52% compared with a similar condenser without radiative cooling. Another example is a PDMS selective emitter combined with a superhydrophobic carbon nanofiber surface, as shown in Fig. 14(f) [85]. This structure enabled a dew harvesting rate of $28.6\,g\,m^{-2}\,h^{-1}$ in a controlled environment at RH of 65% and continuous water harvesting under solar illumination. Although the reported water yields are still relatively low, the potential of these technologies in addressing the global water and energy crisis is particularly appealing. More importantly, the condensed water can be reused for evaporative cooling in the daytime, resulting in a boosted cooling power [157]. As shown in Fig. 14(g), Feng *et al.* [157] proposed a bilayer polymer that consists of a lithium-polyacrylamide hydrogel and a PVDF radiative cooler. In the daytime, due to the synergetic effect of radiative and evaporative cooling, the bilayer polymer realized a remarkable cooling power of $150\,W/m^2$, including $67\,W/m^2$ contributed by evaporation and $84\,W/m^2$ contributed by thermal radiation. During the night, the hydrogel regenerated itself by capturing moisture from the air. This bilayer polymer realized a sustainable cooling power that is less dependent on the weather condition, i.e., it can continuously provide cooling in cloudy weather, which is one of the major setbacks for conventional radiative cooling.

VI. OUTLOOKS AND OPPORTUNITIES

In this review, we discussed the fundamental principles of radiative cooling and recent progress in material selections, system designs, and application developments. Four major components of radiative cooling heat flux, i.e., emitted thermal radiation (P_{rad}), absorbed atmospheric radiation (P_{atm}), absorbed solar irradiation (P_{sun}), and nonradiative heat exchange (P_{nonrad}), were analyzed based on their implementations in recent research works. In general, to obtain an efficient cooling effect, the optical absorption of the emitter needs to be minimized, while its thermal emission (especially within the atmospheric window) needs to be maximized. Different materials and structures have been demonstrated to achieve this critical spectral selectivity using photonic structures, metasurfaces, porous polymers, paints, etc. On the other hand, one can also achieve a high-performance cooling effect using rational system designs, such as solar shelters and tapered beaming and/or waveguide architectures. Building upon these works, practical applications has been summarized, ranging from sustainable building envelopes, thermal management for semiconductor devices, and fabrics for personal thermal management to atmospheric water extraction. However, some major challenges and unresolved issues still require further investigation, as summarized below:

(1) Most reported materials for radiative cooling (especially the scalable polymer materials and paints) are broadband emitters, which are desired in above-ambient temperature conditions such as solar cells. However, engineered narrowband emitters over large scales remain challenging due to the stringent spectral selectivity requirements within the atmospheric window (i.e., 8–14 μm). Future research in large scale and narrowband emitter is strongly encouraged for efficient subambient daytime cooling applications.

(2) Radiative cooling materials are mostly applied under outdoor environments. However, the lifetime and durability of these materials have not been fully examined. For example, authors of only a few studies performed aging tests to reveal the lifetime of their proposed materials under high humidity and hot weather conditions [64,250]. UV stability is also one of the most important features that may affect the durability of materials [172]. It is of great importance for future research to focus on the degradation of the materials under practical environmental conditions.

(3) For atmospheric water harvesting, radiative cooling strategies can be integrated with solar vapor generation systems to accelerate moisture condensation rate [244–249]. However, the overall water productivity needs extensive efforts by engineering surface features. For example, hydrophilic surfaces are normally favorable for dew condensation. However, a hydrophobic surface with a small sliding angle can quickly remove the water droplets, which will also accelerate the water collection rate and condensation process. Introducing micro/nanomorphologies for water clustering and collection is also a promising strategy to facilitate the water harvesting process. How to develop combined hydrophilic and hydrophobic surfaces without sacrificing the radiative cooling performance will be the key in creating atmospheric water harvesting technologies.

(4) Future sustainable building materials require improved energy efficiency and internal environment management [182], depending on the actual weather conditions. Integration of radiative cooling strategies with future building architectures and utilities will require collaborative research efforts related to materials science, thermal management, mechanical engineering, sustainable architecture engineering, etc. [251,252]. For example, the thermal conductivity and thermal capacity of the materials are crucial in insuring high heat transfer efficiency. As a building material, fire resistance is also one of the most important properties to consider. On the other hand, combining thermal storage materials with radiative cooling surfaces also exhibits promising potentials in sustaining a comfortable interior temperature, which can further reduce energy consumption by conventional HVAC utilities [203]. Further development of radiative cooling materials to meet practical building application requirements demands significant research efforts.

In summary, under the emerging pressure of global warming, electricity-free radiative cooling provides a sustainable strategy to reduce energy consumption with minimized carbon emissions to our future daily life.

ACKNOWLEDGMENTS

L.Z., J.R., and Q.G. were partially supported by the Department of Energy (DE-FE0031960). Q.G. acknowledges the financial support by the baseline from PSE, KAUST.

[1] A. Ebrahimi, A. Shayegani, and M. Zarandi, Int. J. Archit. Herit. **15**, 740(2021).

[2] R. Khosla, N. D. Miranda, P. A. Trotter, A. Mazzone, R. Renaldi, C. McElroy, F. Cohen, A. Jani, R. P.

Salazar, and M. McCulloch, Nat. Sustain. **4**, 201 (2021).
[3] U.S. Energy Information Administration, Annual Energy Outlook 2022, https://www.eia.gov/outlooks/aeo/.
[4] X. Yin, R. Yang, G. Tan, and S. Fan, Science **370**, 786 (2020).
[5] J. Rogelj, D. Huppmann, V. Krey, K. Riahi, L. Clarke, M. Gidden, Z. Nicholls, and M. Meinshausen, Nature (London) **573**, 357 (2019).
[6] D. Zhao, A. Aili, Y. Zhai, S. Xu, G. Tan, X. Yin, and R. Yang, Appl. Phys. Rev. **6**, 021306 (2019).
[7] B. Bartoli, S. Catalanotti, B. Coluzzi, V. Cuomo, V. Silvestrini, and G. Troise, Appl. Energy **3**, 267 (1977).
[8] C. G. Granqvist and A. Hjortsberg, Appl. Phys. Lett. **36**, 139 (1980).
[9] C. G. Granqvist, Appl. Opt. **20**, 2606 (1981).
[10] C. G. Granqvist, A. Hjortsberg, and T. S. Eriksson, Thin. Solid. Films **90**, 187 (1982).
[11] S. Catalanotti, V. Cuomo, G. Piro, D. Ruggi, V. Silverstrini, and G. Troise, Sol. Energy **17**, 83 (1975).
[12] A. K. Head, U.S. patent US3043112A (1962).
[13] A. P. Raman, M. A. Anoma, L. Zhu, E. Rephaeli, and S. Fan, Nature (London) **515**, 540 (2014).
[14] S. Fan and W. Li, Nat. Photon. **16**, 182 (2022).
[15] M. M. Hossain and M. Gu, Adv. Sci. **3**, 1500360 (2016).
[16] Z. Li, Q. Chen, Y. Song, B. Zhu, and J. Zhu, Adv. Mater. Technol **5**, 1901007 (2020).
[17] Q. Zhang, S. Wang, X. Wang, Y. Jiang, J. Li, W. Xu, B. Zhu, and J. Zhu, Small Methods **6**, 2101379 (2022).
[18] X. Yu, J. Chan, and C. Chen, Nano Energy **88**, 106259 (2021).
[19] K. T. Lin, J. Han, K. Li, C. Guo, H. Lin, and B. Jia, Nano Energy **80**, 105517 (2021).
[20] M. Chen, D. Pang, X. Chen, H. Yan, and Y. Yang, EcoMat **4**, e12153 (2022).
[21] B. Zhao, M. Hu, X. Ao, N. Chen, and G. Pei, Appl. Energy **236**, 489 (2019).
[22] J. Chen and L. Lu, Sol. Energy **212**, 125 (2020).
[23] M. Hu Suhendri, Y. Su, J. Darkwa, and S. Riffat, Buildings **10**, 215 (2020).
[24] Z. Ma, D. Zhao, C. She, Y. Yang, and R. Yang, Mater. Today Phys. **20**, 100465 (2021).
[25] Y. Peng and Y. Cui, Joule **4**, 724 (2020).
[26] P. Hsu and X. Li, Science **370**, 784 (2020).
[27] D. Sato and N. Yamada, Renew. Sustain. Energy Rev. **104**, 151 (2019).
[28] A. R. Gentle and G. B. Smith, Sol. Energy Mater. Sol. Cells **150**, 39 (2016).
[29] S. Ahmed, Z. Li, M. S. Javed, and T. Ma, Mater. Today Energy **21**, 100776 (2021).
[30] M. J. Moran, H. N. Shapiro, D. D. Boettner, and M. B. Bailey, *Fundamentals of Engineering Thermodynamics*, 8th edition (Wiley, New Jersey, 2014).
[31] Z. Chen, L. Zhu, A. Raman, and S. Fan, Nat. Comm. **7**, 13729 (2016).
[32] B. Orel, M. K. Gunde, and A. Krainer, Sol. Energy **50**, 477 (1993).
[33] A. W. Harrison and M. R. Walton, Sol. Energy **20**, 185 (1978).
[34] T. M. J. Nilsson, W. E. Vargas, G. A. Niklasson, and C. G. Granqvist, Renew. Energy **5**, 310 (1994).
[35] G. A. Niklasson, Physica A **157**, 482 (1989).
[36] J. Mandal, Y. Yang, N. Yu, and A. P. Raman, Joule **4**, 1350 (2020).
[37] C. Yang and C. Wöll, Adv. Phys. X **2**, 373 (2017).
[38] X. Chen, M. He, S. Feng, Z. Xu, H. Peng, S. Shi, C. Liu, and Y. Zhou, Opt. Mater. **120**, 111431 (2021).
[39] X. Li, J. Peoples, Z. Huang, Z. Zhao, J. Qiu, and X. Ruan, Cell Rep. Phys. Sci. **1**, 100221 (2020).
[40] X. Li, J. Peoples, P. Yao, and X. Ruan, ACS Appl. Mater. Interfaces **13**, 21733 (2021).
[41] J. Kischkat, S. Peters, B. Gruska, M. Semtsiv, M. Chashnikova, M. Klinkmüller, O. Fedosenko, S. Machulik, A. Aleksandrova, G. Monastyrskyi *et al.*, Appl. Opt. **51**, 6789 (2012).
[42] Y. Zhai, Y. Ma, S. N. David, D. Zhao, R. Lou, G. Tan, R. Yang, and X. Yin, Science **355**, 1062 (2017).
[43] A. Aili, Z. Y. Wei, Y. Z. Chen, D. L. Zhao, R. Yang, and X. Yin, Mater. Today Phys. **10**, 100127 (2019).
[44] L. Zhou, H. Song, J. Liang, M. Singer, M. Zhou, E. Stegenburgs, N. Zhang, C. Xu, T. Ng, Z. Yu *et al.*, Nat. Sustain. **2**, 718 (2019).
[45] D. Li, X. Liu, W. Li, Z. Lin, B. Zhu, Z. Li, J. Li, B. Li, S. Fan, J. Xie *et al.*, Nat. Nanotechnol. **16**, 153 (2021).
[46] T. Wang, Y. Wu, L. Shi, X. Hu, M. Chen, and L. Wu, Nat. Comm **12**, 365 (2021).
[47] S. Zeng, S. Pian, M. Su, Z. Wang, M. Wu, X. Liu, M. Chen, Y. Xiang, J. Wu, M. Zhang *et al.*, Science **373**, 692 (2021).
[48] U. Banik, A. Agrawal, H. Meddeb, O. Sergeev, N. Reininghaus, M. G. Köhler, K. Gehrke, J. Stührenberg, M. Vehse, M. Sznajder *et al.*, ACS Appl. Mater. Interfaces **13**, 24130 (2021).
[49] X. Yu, W. Song, Q. Yu, S. Li, M. Zhu, Y. Zhang, W. Deng, W. Yang, Z. Huang, X. Bi *et al.*, J. Environ. Sci. **71**, 76 (2018).
[50] R. Zhu, D. Hu, Z. Chen, X. Xu, Y. Zou, L. Wang, and Y. Gu, Nano Lett. **20**, 6974 (2020).
[51] M. Li and C. Coimbra, Int. J. Heat Mass Transfer **135**, 1053 (2019).
[52] M. Dong, N. Chen, X. Zhao, S. Fan, and Z. Chen, Opt. Express **27**, 31587 (2019).
[53] J. Huang, C. Lin, Y. Li, and B. Huang, Int. J. Heat Mass Transfer **186**, 122438 (2022).
[54] A. Berk, P. Conforti, R. Kennett, T. Perkins, F. Hawes, and J. van den Bosch, in *Proceedings of Algorithms and Technologies for Multispectral, Hyperspectral, and Ultraspectral Imagery XX*, Proc. SPIE 9088, edited by M. Velez-Reyes, and F. A. Kruse (SPIE, Baltimore, 2014), Vol. 9088.
[55] J. P. Bijarniya, J. Sarkar, and P. Maiti, J. Cleaner Prod. **274**, 123119 (2020).
[56] C. Y. Tso, K. C. Chan, and C. Chao, Renewable Energy **106**, 52 (2017).
[57] J. Liu, D. Zhang, S. Jiao, Z. Zhou, Z. Zhang, and F. Gao, Sol. Energy Mater. Sol. Cells **208**, 110412 (2020).
[58] H. Zhong, P. Zhang, Y. Li, X. Yang, Y. Zhao, and Z. Wang, ACS Appl. Mater. Interfaces **12**, 51409 (2020).
[59] D. Han, B. F. Ng, and M. P. Wan, Sol. Energy Mater. Sol. Cells **206**, 110270 (2020).
[60] W. Ma, Z. Liu, Z. A. Kudyshev, A. Boltasseva, W. Cai, and Y. Liu, Nat. Photon. **15**, 77 (2021).
[61] J. Rosas, R. Houborg, and M. F. McCabe, Remote Sens. **9**, 988 (2017).

[62] C. Liu, Y. Wu, B. Wang, C. Y. Zhao, and H. Bao, Sol. Energy **183**, 218 (2019).

[63] W. Li, M. Dong, L. Fan, J. J. John, Z. Chen, and S. Fan, ACS Photonics **8**, 269 (2021).

[64] J. Mandal, Y. Fu, A. C. Overvig, M. Jia, K. Sun, N. N. Shi, H. Zhou, X. Xiao, N. Yu, and Y. Yang, Science **362**, 315 (2018).

[65] K. Tang, K. Dong, J. Li, M. P. Gordon, F. G. Reichertz, H. Kim, Y. Rho, Q. Wang, C. Y. Lin, C. P. Grigoropoulos *et al.*, Science **374**, 1504 (2021).

[66] B. Bhatia, A. Leroy, Y. Shen, L. Zhao, M. Gianello, D. Li, T. Gu, J. Hu, M. Soljačić, and E. N. Wang, Nat. Comm. **9**, 5001 (2018).

[67] P. C. Hsu, A. Y. Song, P. B. Catrysse, C. Liu, Y. Peng, J. Xie, S. Fan, and Y. Cui, Science **353**, 1019 (2016).

[68] A. Leroy, B. Bhatia, C. C. Kelsall, A. Castillejo-Cuberos, M. Dicapua H., L. Zhao, L. Zhang, A. M. Guzman, and E. N. Wang, Sci. Adv. **5**, eaat 9480 (2019).

[69] Z. Wang, D. Kortge, J. Zhu, Z. Zhou, H. Torsina, C. Lee, and P. Bermel, Joule **4**, 2702 (2020).

[70] Z. Li, S. Ahmed, and T. Ma, Solar RRL **5**, 2000735 (2021).

[71] T. Li, Y. Zhai, S. He, W. Gan, Z. Wei, M. Heidarinejad, D. Dalgo, R. Mi, X. Zhao, J. Song *et al.*, Science **364**, 760 (2019).

[72] S. Wang, T. Jiang, Y. Meng, R. Yang, G. Tan, and Y. Long, Science **374**, 1501 (2021).

[73] D. Zhao, A. Aili, Y. Zhai, J. Lu, D. Kidd, G. Tan, X. Yin, and R. Yang, Joule **3**, 111 (2019).

[74] J. Mandal, M. Jia, A. Overvig, Y. Fu, E. Che, N. Yu, and Y. Yang, Joule **3**, 3088 (2019).

[75] X. Xue, M. Qiu, Y. Li, Q. M. Zhang, S. Li, Z. Yang, C. Feng, W. Zhang, J. G. Dai, D. Lei *et al.*, Adv. Mater. **32**, 1906751 (2020).

[76] C. Lin, Y. Li, C. Chi, Y. S. Kwon, J. Huang, Z. Wu, J. Zheng, G. Liu, C. Y. Tso, C. Y. H. Chao *et al.*, Adv. Mater. **34**, 2109350 (2022).

[77] L. Cai, Y. Peng, J. Xu, C. Zhou, C. Zhou, P. Wu, D. Lin, S. Fan, and Y. Cui, Joule **3**, 1478 (2019).

[78] L. Cai, A. Y. Song, W. Li, P. C. Hsu, D. Lin, P. B. Catrysse, Y. Liu, Y. Peng, J. Chen, H. Wang *et al.*,, Adv. Mater. **30**, 1802152 (2018).

[79] Z. Chen, L. Zhu, W. Li, and S. Fan, Joule **3**, 101 (2019).

[80] M. A. Kats, R. Blanchard, P. Genevet, and F. Capasso, Nat. Mater. **12**, 20 (2013).

[81] M. A. Kats, S. J. Byrnes, R. Blanchard, M. Kolle, P. Genevet, J. Aizenberg, and F. Capasso, Appl. Phys. Lett **103**, 101104 (2013).

[82] M. A. Kats and F. Capasso, Appl. Phys. Lett **105**, 131108 (2014).

[83] A. P. Raman, W. Li, and S. Fan, Joule **3**, 2679 (2019).

[84] Y. Li, C. Lin, J. Huang, C. Chi, and B. Huang, Global Challenges **5**, 2000058 (2021).

[85] I. Haechler, H. Park, G. Schnoering, T. Gulich, M. Rohner, A. Tripathy, A. Milionis, T. M. Schutzius, and D. Poulikakos, Sci. Adv. **7**, eabf3978 (2021).

[86] H. Kim, S. R. Rao, E. A. Kapustin, L. Zhao, S. Yang, O. M. Yaghi, and E. N. Wang, Nat. Comm. **9**, 1191 (2018).

[87] H. Ma, K. Yao, S. Dou, M. Xiao, M. Dai, L. Wang, H. Zhao, J. Zhao, Y. Li, and Y. Zhan, Sol. Energy Mater. Sol. Cells **212**, 110584 (2020).

[88] K. Yao, H. Ma, M. Huang, H. Zhao, J. Zhao, Y. Li, S. Dou, and Y. Zhan, ACS Appl. Nano Mater. **2**, 5512 (2019).

[89] D. Chae, M. Kim, P. H. Jung, S. Son, J. Seo, Y. Liu, B. J. Lee, and H. Lee, ACS Appl. Mater. Interfaces **12**, 8073 (2020).

[90] J. Kou, Z. Jurado, Z. Chen, S. Fan, and A. J. Minnich, ACS Photonics **4**, 626 (2017).

[91] H. Yuan, C. Yang, X. Zheng, W. Mu, Z. Wang, W. Yuan, Y. Zhang, C. Chen, X. Liu, and W. Shen, Opt. Express **26**, 27885 (2018).

[92] Y. Zhu, D. Wang, C. Fang, P. He, and Y. H. Ye, Polymers **11**, 1203 (2019).

[93] A. Kumar and A. Chowdhury, Sol. Energy **201**, 751 (2020).

[94] G. Bakan, S. Ayas, M. Serhatlioglu, C. Elbuken, and A. Dana, Adv. Opt. Mater. **6**, 1800613 (2018).

[95] O. Ilic, C. M. Went, and H. A. Atwater, Nano Lett. **18**, 5583 (2018).

[96] Y. Shi, Wei. Li, A. Raman, and S. Fan, ACS Photonics **5**. 684 (2018).

[97] M. Chen, D. Pang, J. Mandal, X. Chen, H. Yan, Y. He, N. Yu, and Y. Yang, Nano Lett. **21**, 1412 (2021).

[98] P. You, X. Li, Y. Huang, X. Ma, M. Pu, Y. Guo, and X. Luo, Materials **13**, 2885 (2020).

[99] W. Xi, Y. Liu, W. Zhao, R. Hu, and X. Luo, Int. J. Therm. Sci. **170**, 107172 (2021).

[100] L. Zhou, J. Rada, H. Song, B. Ooi, Z. Yu, and Q. Gan, J. Photonics Energy **11**, 042107 (2021).

[101] G. J. Lee, Y. J. Kim, H. M. Kim, Y. J. Yoo, and Y. M. Song, Adv. Opt. Mater. **6**, 1800707 (2018).

[102] Y. Zhu, H. Luo, C. Yang, B. Qin, P. Ghosh, S. Kaur, W. Shen, M. Qiu, P. Belov, and Q. Li, Light Sci. Appl. **11**, 122 (2022).

[103] C. C. Tsai, R. A. Childers, N. N. Shi, C. Ren, J. N. Pelaez, G. D. Bernard, N. E. Pierce, and N. Yu, Nat. Comm. **11**, 551 (2020).

[104] N. N. Shi, C. C. Tsai, F. Camino, G. D. Bernard, N. Yu, and R. Wehner, Science **349**, 298 (2015).

[105] L. Zhu, A. P. Raman, and S. Fan, Proc. Natl Acad. Sci. **112**, 12282 (2015).

[106] H. Akbari, P. Berdahl, R. Levinson, and S. Wiel, *Cool Color Roofing Materials* (Lawrence Berkeley National Laboratory, Berkeley, 2006).

[107] W. Li, Y. Shi, Z. Chen, and S. Fan, Nat. Comm. **9**, 4240 (2018).

[108] L. Maigyte and K. Staliunas, Appl. Phys. Rev. **2**, 011102 (2015).

[109] V. Berger, Opt. Mater. **11**, 131 (1999).

[110] E. Rephaeli, A. Raman, and S. Fan, Nano Lett. **13**, 1457 (2013).

[111] H. H. Kim, E. Im, and S. Lee, Langmuir **36**, 6589 (2020).

[112] P. Li, A. Wang, J. Fan, Q. Kang, P. Jiang, H. Bao, and X. Huang, Adv. Funct. Mater. **32**, 2109542 (2022).

[113] D. Wu, C. Liu, Z. Xu, Y. Liu, Z. Yu, L. Yu, L. Chen, R. Li, R. Ma, and H. Ye, Mater. Des. **139**, 104 (2018).

[114] B. Zhao, M. Hu, X. Ao, Q. Xuan, and G. Pei, Sol. Energy Mater. Sol. Cells **178**, 266 (2018).

[115] S. Atiganyanun, J. B. Plumley, S. J. Han, K. Hsu, J. Cytrynbaum, T. L. Peng, S. M. Han, and S. E. Han, ACS Photonics **5**, 1181 (2018).

[116] M. M. Hossain, B. Jia, and M. Gu, Adv. Opt. Mater. **3**, 1047 (2015).

[117] M. Gao, X. Han, F. Chen, W. Zhou, P. Liu, Y. Shan, Y. Chen, J. Li, R. Zhang, S. Wang *et al.*, Sol. Energy Mater. Sol. Cells **200**, 110013 (2019).

[118] H. Zhu, Q. Li, C. Tao, Y. Hong, Z. Xu, W. Shen, S. Kaur, P. Ghosh, and M. Qiu, Nat. Comm. **12**, 1805 (2021).

[119] X. Wang, X. Liu, Z. Li, H. Zhang, Z. Yang, H. Zhou, and T. Fan, Adv. Funct. Mater. **30**, 1907562 (2020).

[120] L. Zhou, J. Zhao, H. Huang, F. Nan, G. Zhou, and Q. Ou, ACS Photonics **8**, 3301 (2021).

[121] S. Y. Heo, G. J. Lee, D. H. Kim, Y. J. Kim, S. Ishii, M. S. Kim, T. J. Seok, B. J. Lee, H. Lee, and Y. M. Song, Sci. Adv. **6**, eabb1906 (2020).

[122] S. Fan, Joule **1**, 264 (2107).

[123] W. Li and S. Fan, Opt. Express **26**, 15995 (2018).

[124] K. C. S. Ly, X. Liu, X. Song, C. Xiao, P. Wang, H. Zhou, and T. Fan, Adv. Funct. Mater. **32**, 2203789 (2022).

[125] Z. Jiang and J. H. Pikul, Nat. Mater. **20**, 1512 (2021).

[126] J. Rada, H. Hu, L. Zhou, J. Zeng, H. Song, X. Zeng, S. Shimul, W. Fan, Q. Zhan, W. Li *et al.*, Appl. Mater. Today **24**, 101146 (2021).

[127] Y. Cui, H. Gong, Y. Wang, D. Li, and H. Bai, Adv. Mater. **30**, 1706807 (2018).

[128] A. Krishna, X. Nie, A. D. Warren, J. E. L. Bousquets, A. D. Briscoe, and J. Lee, Proc. Natl Acad. Sci. USA **117**, 1566 (2020).

[129] P. Vukusic and J. R. Sambles, Nature (London) **424**, 852 (2003).

[130] H. Zhang, K. C. S. Ly, X. Liu, Z. Chen, M. Yan, Z. Wu, X. Wang, Y. Zheng, H. Zhou, and T. Fan, Proc. Natl Acad. Sci. USA **117**, 14657 (2020).

[131] Z. Cheng, H. Han, F. Wang, Y. Yan, X. Shi, H. Liang, X. Zhang, and Y. Shuai, Nano Energy **89**, 106377 (2021).

[132] X. Liu, C. Xiao, P. Wang, M. Yan, H. Wang, P. Xie, G. Liu, H. Zhou, D. Zhang, and T. Fan, Adv. Opt. Mater. **9**, 2101151 (2021).

[133] S. Y. Jeong, C. Y. Tso, Y. M. Wong, C. Y. H. Chao, and B. Huang, Sol. Energy Mater. Sol. Cells **206**, 110296 (2020).

[134] B. Yu, Z. Huang, D. Fang, S. Yu, T. Fu, Y. Tang, and Z. Li, Adv. Mater. Interfaces **9**, 2101485 (2022).

[135] C. Zhou, I. Julianri, S. Wang, S. H. Chan, M. Li, and Y. Long, ACS Mater. Lett. **3**, 883 (2021).

[136] S. Chen, W. Liu, Z. Li, H. Cheng, and J. Tian, Adv. Mater. **32**, 1805912 (2020).

[137] G. M. Akselrod, J. Huang, T. B. Hoang, P. T. Bowen, L. Su, D. R. Smith, and M. H. Mikkelsen, Adv. Mater. **27**, 8028 (2015).

[138] M. Khorasaninejad and F. Capasso, Science **358**, eaam8100 (2017).

[139] N. Yu and F. Capasso, Nat. Mater. **13**, 139 (2014).

[140] J. W. Cho, S. J. Park, S. J. Park, Y. B. Kim, Y. J. Moon, and S. K. Kim, Nano Lett. **9**, 3974 (2021).

[141] C. Zou, G. Ren, M. M. Hossain, S. Nirantar, W. Withayachumnankul, T. Ahmed, M. Bhaskaran, S. Sriram, M. Gu, and C. Fumeaux, Adv. Opt. Mater. **5**, 1700460 (2017).

[142] Z. Qin, C. Zhang, Z. Liang, D. Meng, X. Shi, and F. Yang, Adv. Photonics Res. **3**, 2100215 (2022).

[143] W. Yu, Y. Lu, X. Chen, H. Xu, J. Shao, X. Chen, Y. Sun, J. Hao, and N. Dai, Adv. Opt. Mater. **7**, 1900841 (2019).

[144] G. J. Lee, D. H. Kim, S. Y. Heo, and Y. M. Song, ACS Appl. Mater. Interfaces **12**, 53206 (2020).

[145] D. H. Kim, G. J. Lee, S. Y. Heo, I. S. Kang, and Y. M. Song, Sol. Energy Mater. Sol. Cells **230**, 111173 (2021).

[146] W. Wang, Z. Zhao, Q. Zou, B. Hong, W. Zhang, and G. P. Wang, J. Mater. Chem. C **8**, 3192 (2020).

[147] M. Ono, K. Chen, W. Li, and S. Fan, Opt. Express **26**, A777 (2018).

[148] L. Long, S. Taylor, and L. Wang, ACS Photonics **7**, 2219 (2020).

[149] K. Sun, C. A. Riedel, Y. Wang, A. Urbani, M. Simeoni, S. Mengali, M. Zalkovskij, B. Bilenberg, C. H. de Groot, and O. L. Muskens, ACS Photonics **5**, 495 (2018).

[150] T. Wriedt, *Mie Theory: A Review* (Springer, Bremen, 2012), Vol. 169, p. 53–71.

[151] Y. Fu, J. Yang, Y. S. Su, W. Du, and Y. G. Ma, Sol. Energy Mater. Sol. Cells **191**, 50 (2019).

[152] B. Xiang, R. Zhang, Y. Luo, S. Zhang, L. Xu, H. Min, S. Tang, and X. Meng, Nano Energy **81**, 105600 (2021).

[153] D. Lee, M. Go, S. Son, M. Kim, T. Badloe, H. Lee, J. K. Kim, and J. Rho, Nano Energy **79**, 105426 (2021).

[154] S. Son, Y. Liu, D. Chae, and H. Lee, ACS Appl. Mater. Interfaces **12**, 57832 (2020).

[155] H. D. Wang, C. H. Xue, X. J. Guo, B. Y. Liu, Z. Y. Ji, M. C. Huang, and S. T. Jia, Appl. Mater. Today **24**, 101100 (2021).

[156] J. Wang, J. Sun, T. Guo, H. Zhang, M. Xie, J. Yang, X. Jiang, Z. Chu, D. Liu, and S. Bai, Adv. Mater. Technol. **7**, 2100528 (2022).

[157] C. Feng, P. Yang, H. Liu, M. Mao, Y. Liu, T. Xue, J. Fu, T. Cheng, X. Hu, H. J. Fan *et al.*, Nano Energy **85**, 105971 (2021).

[158] K. Zhou, W. Li, B. B. Patel, R. Tao, Y. Chang, S. Fan, Y. Diao, and L. Cai, Nano Lett. **21**, 1493 (2021).

[159] J. Li, Y. Liang, W. Li, N. Xu, B. Zhu, Z. Wu, X. Wang, S. Fan, M. Wang, and J. Zhu, Sci. Adv. **8**, eabj9756 (2022).

[160] J. Wu, J. He, K. Yin, Z. Zhu, S. Xiao, Z. Wu, and J. A. Duan, Nano Lett. **21**, 4209 (2021).

[161] H. Kim, S. McSherry, B. Brown, and A. Lenert, ACS Appl. Mater. Interfaces **12**, 43553 (2020).

[162] W. Gao, Z. Lei, K. Wu, and Y. Chen, Adv. Funct. Mater. **31**, 2100535 (2021).

[163] N. Li, J. Wang, D. Liu, X. Huang, Z. Xu, C. Zhang, Z. Zhang, and M. Zhong, Sol. Energy Mater. Sol. Cells **194**, 103 (2019).

[164] J. Huang, D. Fan, and Q. Li, Mater. Today Energy **25**, 100955 (2022).

[165] H. Zhao, Q. Sun, J. Zhou, X. Deng, and J. Cui, Adv. Mater. **32**, 2000870 (2020).

[166] Y. Chen, B. Dang, J. Fu, C. Wang, C. Li, Q. Sun, and H. Li, Nano Lett. **21**, 397 (2021).

[167] S. Zhong, L. Yi, J. Zhang, T. Xu, L. Xu, X. Zhang, T. Zuo, and Y. Cai, Chem. Eng. J. **407**, 127104 (2021).

[168] Y. Tian, X. Liu, Z. Wang, J. Li, Y. Mu, S. Zhou, F. Chen, M. L. Minus, G. Xiao, and Y. Zheng, Nano Energy **96**, 107085 (2022).

[169] Y. Tian, X. Liu, J. Li, A. Caratenuto, S. Zhou, Y. Deng, G. Xiao, M. L. Minus, and Y. Zheng, Appl. Mater. Today **24**, 101103 (2021).

[170] J. J. Fernandez, H. Yang, L. Schertel, G. L. Whitworth, P. D. Garcia, S. Vignolini, and C. M. S. Torres, Adv. Sci. **9**, 2104758 (2022).

[171] H. Zhong, Y. Li, P. Zhang, S. Gao, B. Liu, Y. Wang, T. Meng, Y. Zhou, H. Hou, C. Xue *et al.*, ACS Nano **15**, 10076 (2021).

[172] L. Zhou, J. Rada, H. Zhang, H. Song, S. Mirniaharikandi, B. S. Ooi, and Q. Gan, Adv. Sc. **8**, 2102502 (2021).

[173] X. Yue, H. Wu, T. Zhang, D. Yang, and F. Qiu, Energy **245**, 123287 (2022).

[174] Y. Chen, J. Mandal, W. Li, A. S. Washington, C. C. Tsai, W. Huang, S. Shrestha, N. Yu, R. P. S. Han, A. Cao *et al.*, Sci. Adv. **6**, eaaz5413 (2020).

[175] W. Huang, Y. Chen, Y. Luo, J. Mandal, W. Li, M. Chen, C. C. Tsai, Z. Shan, N. Yu, and Y. Yang, Adv. Funct. Mater. **31**, 2010334 (2021).

[176] D. Chae, S. Son, H. Lim, P. H. Jung, J. Ha, and H. Lee, Mater. Today Phys. **18**, 100389 (2021).

[177] Y. Zhao, D. Pang, M. Chen, Z. Chen, and H. Yan, Appl. Mater. Today **26**, 101298 (2022).

[178] Z. Tong, J. Peoples, X. Li, X. Yang, H. Bao, and X. Ruan, Mater. Today Phys. **24**, 100658 (2022).

[179] J. Zhang, J. Yuan, J. Liu, Z. Zhou, J. Sui, J. Xing, and J. Zuo, Renew. Sustain. Energy Rev. **143**, 110959 (2021).

[180] L. Zhou, H. Song, N. Zhang, J. Rada, M. Singer, H. Zhang, B. S. Ooi, Z. Yu, and Q. Gan, Cell Rep. Phys. Sci. **2**, 100338 (2021).

[181] J. Peoples, Y. W. Hung, X. Li, D. Gallagher, N. Fruehe, M. Pottschmidt, C. Breseman, C. Adams, A. Yuksel, J. Braun *et al.*, Appl. Energy **310**, 118368 (2022).

[182] S. Cui, A. Odukomaiya, and J. Vidal, MRS Bull. **46**, 1176 (2021).

[183] E. A. Goldstein, A. P. Raman, and S. Fan, Nat. Energy **2**, 17143 (2017).

[184] H. Apostoleris, M. Stefancich, and M. Chiesa, Nat. Energy **1**, 16018 (2016).

[185] L. Carlosena, A. R. Pardo, J. Feng, O. Irulegi, R. J. H. Minguillón, and M. Santamouris, Sol. Energy **208**, 430 (2020).

[186] N. Wang, Y. Lv, D. Zhao, W. Zhao, J. Xu, and R. Yang, Mater. Today Energy **24**, 100927 (2022).

[187] K. Zhang, D. Zhao, X. Yin, R. Yang, and G. Tan, Appl. Energy **224**, 371 (2018).

[188] E. Teitelbaum, K. W. Chen, D. Aviv, K. Bradford, L. Ruefenacht, D. Sheppard, M. Teitelbaum, F. Meggers, J. Pantelic, and A. Rysanek, Proc. Natl Acad. Sci. USA **117**, 21162 (2020).

[189] Y. Liu, Y. Tian, X. Liu, F. Chen, A. Caratenuto, and Y. Zheng, Appl. Phys. Lett. **120**, 171704 (2022).

[190] T. Wang, Y. Zhang, M. Chen, M. Gu, and L. Wu, Cell Rep. Phys. Sci. **3**, 100782 (2022).

[191] X. Zhao, A. Aili, D. Zhao, D. Xu, X. Yin, and R. Yang, Cell Rep. Phys. Sci. **3**, 100853 (2022).

[192] Y. Sun, Y. Ji, M. Javed, X. Li, Z. Fan, Y. Wang, Z. Cai, and B. Xu, Adv. Mater. Technol. **7**, 2100803 (2022).

[193] T. Hu, T. H. Kwan, and G. Pei, Renew. Energy **186**, 831 (2022).

[194] B. Zhao, M. Hu, Q. Xuan, T. H. Kwan, Y. N. Dabwan, and G. Pei, Sol. Energy Mater. Sol. Cells **235**, 111457 (2022).

[195] X. Li, B. Sun, C. Sui, A. Nandi, H. Fang, Y. Peng, G. Tan, and P. C. Hsu, Nat. Comm. **11**, 6101 (2020).

[196] Q. Zhai and Q. Zhu, Sol. Energy Mater. Sol. Cells **228**, 111117 (2021).

[197] G. Chen, Y. Wang, J. Qiu, J. Cao, Y. Zou, S. Wang, J. Ouyang, D. Jia, and Y. Zhou, J. Mater. Sci. Technol. **90**, 76 (2021).

[198] B. Zhao, C. Wang, M. Hu, X. Ao, J. Liu, Q. Xuan, and G. Pei, Energy **238**, 121761 (2022).

[199] G. Wei, D. Yang, T. Zhang, X. Yue, and F. Qiu, Sol. Energy Mater. Sol. Cells **202**, 110125 (2019).

[200] B. Y. Liu, C. H. Xue, H. M. Zhong, X. J. Guo, H. D. Wang, H. G. Li, M. M. Du, M. C. Huang, R. X. Wei, L. G. Song, B. Chang, and Z. Wang, J. Mater. Chem. A **9**, 24276 (2021).

[201] B. Zhao, X. Yue, Q. Tian, F. Qiu, and T. Zhang, Cellulose **29**, 1981 (2022).

[202] Y. Tian, H. Shao, X. Liu, F. Chen, Y. Li, C. Tang, and Y. Zheng, ACS Appl. Mater. Interfaces **13**, 22521 (2021).

[203] G. Paranjothi, A. Odukomaiya, S. Cui, and A. Bulk, Energy Build. **253**, 111372 (2021).

[204] L. Xu, W. Liu, H. Liu, C. Ke, M. Wang, C. Zhang, E. Aydin, M. A. Aswad, K. Kotsovos, I. Gereige *et al.*, Joule **5**, 631 (2021).

[205] T. J. Hsiao, T. Eyassu, K. Henderson, T. Kim, and C. T. Lin, Nanotechnology **24**, 395401 (2013).

[206] X. Liu, M. H. Hu, C. G. Caneau, R. Bhat, and C. E. Zah, IEEE Trans. Compon. Packag. Technol. **29**, 268 (2006).

[207] L. Zhu, A. Raman, K. X. Wang, M. A. Anoma, and S. Fan, Optica **1**, 32 (2014).

[208] Y. Lu, Z. Chen, L. Ai, X. Zhang, J. Zhang, J. Li, W. Wang, R. Tan, N. Dai, and W. Song, Solar RRL **1**, 1700084 (2017).

[209] E. Lee and T. Luo, Sol. Energy Mater. Sol. Cells **194**, 222 (2019).

[210] J. J. Fernandez, G. L. Whitworth, J. A. Pariente, A. Blanco, P. D. Garcia, C. Lopez, and C. M. S. Torres, Small **15**, 1905290 (2019).

[211] G. Perrakis, A. C. Tasolamprou, G. Kenanakis, E. N. Economou, S. Tzortzakis, and M. Kafesaki, Opt. Express **28**, 18548 (2020).

[212] B. Zhao, M. Hu, X. Ao, and G. Pei, Sol. Energy **176**, 248 (2018).

[213] W. Li, Y. Shi, K. Chen, L. Zhu, and S. Fan, ACS Photonics **4**, 774 (2017).

[214] Z. Huang and X. Ruan, Int. J. Heat Mass Transfer **104**, 890 (2017).

[215] K. Wang, G. Luo, X. Guo, S. Li, Z. Liu, and C. Yang, Sol. Energy **225**, 245 (2021).

[216] B. Zhao, K. Lu, M. Hu, J. Liu, L. Wu, C. Xu, Q. Xuan, and G. Pei, Renew. Energy **191**, 662 (2022).

[217] S. Ahmed, S. Li, Z. Li, G. Xiao, and T. Ma, Appl. Energy **308**, 118363 (2022).

[218] H. Tang, Z. Zhou, S. Jiao, Y. Zhang, S. Li, D. Zhang, J. Zhang, J. Liu, and D. Zhao, Sol. Energy Mater. Sol. Cells **235**, 111498 (2022).

[219] J. N. Munday and T. Safi, in *2016 IEEE 43rd Photovoltaic Specialists Conference (PVSC)* (IEEE, Portland, 2016), pp. 1125.

[220] U. Banik, K. Sasaki, N. Reininghaus, K. Gehrke, M. Vehse, M. Sznajder, T. Sproewitz, and C. Agert, Sol. Energy Mater. Sol. Cells **209**, 110456 (2020).

[221] K. W. Lee, W. Lim, M. S. Jeon, H. Jang, J. Hwang, C. H. Lee, and D. R. Kim, Adv. Funct. Mater. **32**, 2105882 (2022).

[222] X. Huang, W. Li, H. Fu, D. Li, C. Zhang, H. Chen, Y. Fang, K. Fu, S. P. DenBaars, S. Nakamura *et al.*, ACS Photonics **6**, 2096 (2019).

[223] L. Fan, W. Li, W. Jin, M. Orenstein, and S. Fan, Opt. Express **28**, 25460 (2020).

[224] W. Ren, Y. Sun, D. Zhao, A. Aili, S. Zhang, C. Shi, J. Zhang, H. Geng, J. Zhang, L. Zhang *et al.*, Sci. Adv. **7**, eabe0586 (2021).

[225] Z. Zhan, M. ElKabbash, Z. Li, X. Li, J. Zhang, J. Rutledge, S. Singh, and C. Guo, Nano Energy **65**, 104060 (2019).

[226] W. Li, S. Buddhiraju, and S. Fan, Light Sci. Appl. **9**, 68 (2020).
[227] S. Ishii, T. D. Dao, and T. Nagao, Appl. Phys. Lett. **117**, 013901 (2020).
[228] Y. Liu, S. Hou, X. Wang, L. Yin, Z. Wu, X. Wang, J. Mao, J. Sui, X. Liu, Q. Zhang *et al.*, Small **18**, 2106875 (2022).
[229] B. Zhao, G. Pei, and A. P. Raman, Appl. Phys. Lett. **117**, 163903 (2020).
[230] S. Khan, J. Kim, K. Roh, G. Park, and W. Kim, Nano Energy **87**, 106180 (2021).
[231] Y. Peng, J. Chen, A. Y. Song, P. B. Catrysse, P. C. Hsu, L. Cai, B. Liu, Y. Zhu, G. Zhou, D. S. Wu *et al.*, Nat. Sustain. **1**, 105 (2018).
[232] X. Shan, L. Liu, Y. Wu, D. Yuan, J. Wang, C. Zhang, and J. Wang, Adv. Sci. **9**, 2201190 (2022).
[233] B. Zhu, W. Li, Q. Zhang, D. Li, X. Liu, Y. Wang, N. Xu, Z. Wu, J. Li, X. Li *et al.*, Nat. Nanotech. **16**, 1342 (2021).
[234] L. Cai, A. Y. Song, P. Wu, P. C. Hsu, Y. Peng, J. Chen, C. Liu, P. B. Catrysse, Y. Liu, A. Yang *et al.*, Nat. Comm. **8**, 496 (2017).
[235] G. Kim, K. Park, K. Hwang, C. Choi, Z. Zheng, R. Seydel, A. Coza, and S. Jin, Nano Energy **82**, 105715 (2021).
[236] D. Miao, N. Cheng, X. Wang, J. Yu, and B. Ding, Nano Lett. **22**, 680 (2022).
[237] X. Zhang, W. Yang, Z. Shao, Y. Li, Y. Su, Q. Zhang, C. Hou, and H. Wang, ACS Nano **16**, 2188 (2022).
[238] R. Xiao, C. Hou, W. Yang, Y. Su, Y. Li, Q. Zhang, P. Gao, and H. Wang, ACS Appl. Mater. Interfaces **11**, 44673 (2019).
[239] Y. N. Song, M. Q. Lei, J. Lei, and Z. M. Li, Adv. Mater. Technol. **5**, 2000287 (2020).
[240] Y. Fang, X. Zhao, G. Chen, T. Tat, and J. Chen, Joule **5**, 752 (2021).
[241] H. Fang, W. Xie, X. Li, K. Fan, Y. T. Lai, B. Sun, S. Bai, W. J. Padilla, and P. C. Hsu, Nano Lett. **21**, 4106 (2021).
[242] P. C. Hsu, C. Liu, A. Y. Song, Z. Zhang, Y. Peng, J. Xie, K. Liu, C. L. Wu, P. B. Catrysse, L. Cai *et al.*, Sci. Adv. **3**, e1700895 (2017).
[243] X. Li, B. Ma, J. Dai, C. Sui, D. Pande, D. R. Smith, L. C. Brinson, and P. C. Hsu, Sci. Adv. **7**, eabj7906 (2021).
[244] Y. Zhang, W. Zhu, C. Zhang, J. Peoples, X. Li, A. L. Felicelli, X. Shan, D. M. Warsinger, T. B. Tasciuc, X. Ruan *et al.*, Nano Lett. **22**, 2618 (2022).
[245] M. Dong, Z. Zhang, Y. Shi, X. Zhao, S. Fan, and Z. Chen, Nanoscale Microscale Thermophys. Eng. **24**, 43 (2020).
[246] M. Zhou, H. Song, X. Xu, A. Shahsafi, Y. Qu, Z. Xia, Z. Ma, M. A. Kats, J. Zhu, B. S. Ooi *et al.*, Proc. Natl. Acad. Sci. USA **118**, e2019292118 (2021).
[247] M. Chen, Z. Yi, S. Tao, S. Wang, Z. Fang, C. Lu, and Z. Xu, Global Challenges **4**, 1900094 (2020).
[248] C. Liu, J. Fan, and H. Bao, Sol. Energy Mater. Sol. Cells **216**, 110700 (2020).
[249] J. Xu, J. Zhang, B. Fu, C. Song, W. Shang, P. Tao, and T. Deng, ACS Appl. Mater. Interfaces **12**, 47612 (2020).
[250] H. Liu, H. Kang, X. Jia, X. Qiao, W. Qin, and X. Wu, Adv. Mater. Technol. **7**, 2101583 (2022).
[251] X. Li, W. Xie, C. Sui, and P. C. Hsu, ACS Mater. Lett. **2**, 1624 (2020).
[252] D. A. Suhamad and S. P. Martana, IOP Conf. Ser.: Mater. Sci. Eng. **879**, 012146 (2020).